1 Geochemical and mineralogical proxies beyond temperature: autumn seasons trapped in 2 freshwater nacre 3 4 Gabriela A. Farfan,^{1,*} Emma S. Bullock,² Chunhui Zhou,³ and John W. Valley⁴ 5 6 ¹Department of Mineral Sciences, National Museum of Natural History, Smithsonian Institution, 7 Washington, DC, 20560 USA 8 ²Earth and Planets Laboratory, Carnegie Institution for Science, Washington, DC, 20015 USA 9 ³Gemological Institute of America, New York, NY 10036 USA 10 ⁴Department of Geoscience, University of Wisconsin, Madison, WI 53706 USA 11 *Corresponding Author: farfang@si.edu, https://orcid.org/0000-0001-5204-7044 12 13 KEYWORDS: nacre, environmental biomineralogy, carbonates, cathodoluminescence, Raman 14 spectroscopy 15 16 Final Publication: 17 Farfan GA, Bullock ES, Zhou C, Valley JW (2023) Geochemical and mineralogical proxies beyond 18 temperature: autumn seasons trapped in freshwater nacre, Geochim Cosmochim Acta. 355: 126-137. 19 doi.org/10.1016/j.gca.2023.06.033 20 21 **Abstract** 22 Measurements of trace element chemistry, mineralogy, and isotope geochemistry are rarely 23 combined with known environmental data to provide a more complete story about how 24 environmental conditions are recorded in biomineral carbonates. Here, cultured (farmed) pearls

serve as relatively pristine time capsules to study these geochemical and mineral-based proxies. Cathodoluminescence (CL) imaging and Raman spectroscopic mapping on the µm-scale reveals that heterogeneous crystal bonding environments, geochemistry, and organic contents across the growth history of a freshwater pearl reflect environmental shifts in Kentucky Lake, TN, USA. A major CL peak at 551 nm aligns with increased manganese and organic contents and correlates with lake conductivity and alkalinity data. These CL features are temporally offset from previous 10- μ m-scale aragonite nacre oxygen isotope measurements ($\delta^{18}O_{Arg}$) that record periods of minimum lake temperatures in winter seasons. Thus, we suggest that these trace element and organic features represent autumn or spring rainy seasons that experience lake turnover events and more land runoff rich in Mn and nutrients, increasing aragonite-bound Mn and organic contents in the nacre. This 551 nm signal is absent in Mn-poor saltwater pearl nacre. A second CL peak at 444 nm shows different heterogeneous features likely due to crystal structure shifts, as evidenced by correlations to a Raman map of translational (T): librational (L) mode height ratios typically signaling changes in nacre tablet orientation. Thus, we show that µm-scale CL and Raman mapping may serve as complementary environmental proxies to novel SIMS-based $\delta^{18}O_{Arg}$ temperature proxies in order to capture additional information about local lake environments at seasonal to sub-seasonal temporal resolutions.

42

43

44

45

46

47

25

26

27

28

29

30

31

32

33

34

35

36

37

38

39

40

41

1. Introduction

Mollusk nacre is a unique biomineral that is of interest across the scientific fields of geochemistry, biomineralogy, materials science, gemology, paleoclimate, and environmental science. Nacre is composed of tablets of aragonite (CaCO₃) stacked together like bricks and interlaid with biological molecules, such as β -chitin and acidic proteins, that serve as the mortar

(Addadi and Weiner, 1997; Levi-Kalisman et al., 2001). Containing up to ~5 wt % organics (Gilbert et al., 2005), being a composite material gives nacre incredible physical properties compared to its abiological aragonite counterparts, such as additional toughness, pearlescent luster, and self-healing symmetry properties (Addadi et al., 2006; Espinosa et al., 2011; Barthelat et al., 2016; Gim et al., 2019; 2021). Like tree rings, the layered nature of nacre preserves a chemical and mineralogical record of environmental conditions during growth. Thus, nacre lends itself to being used as an archive for paleoproxies, such as temperature proxies based on oxygen isotopes (Linzmeier et al., 2018; Rousseau and Rollion-Bard, 2012; Farfan et al., 2021), tablet thickness (Olson et al., 2012; Gilbert et al., 2017), and even tablet orientation (Olson and Gilbert, 2012; Farfan et al., 2021). Empirically-based biomineral, chemical, and isotope paleoproxies are extensively used to trace past climate, yet the relationship between isotopic compositions and trace element chemistry and how they relate to kinetics of crystallization, crystal structure, and trapped organic molecules is still an active topic of research across a range of biomineralizing organisms (Thompson, 2022). A combined mineralogical-geochemical approach offers a new perspective to help understand how these proxies relate to crystal chemistry and structure. Modern farmed ("cultured") freshwater pearls provide relatively pristine continuous records of nacre of known ages that can aid in our understanding of these relationships. In this study, we explore how trace element and organic signals are trapped in natural nacre from a previously-studied freshwater cultured pearl from Kentucky Lake, Tennessee, USA. Measurements of pearl mineralogy (Raman spectroscopy mapping of carbonate vibrational modes, cathodoluminescence (CL) mapping), trace elements (CL mapping, electron microprobe

geochemical mapping), and organic contents (Raman spectroscopy background fluorescence) are

captured at μm-resolution and compared to previously published nacre δ¹⁸O_{Arg}, OH/O and tablet

48

49

50

51

52

53

54

55

56

57

58

59

60

61

62

63

64

65

66

67

68

69

thickness measurements from Farfan et al. (2021). It is important to note that here we only investigated one freshwater pearl because of the extensive time investment required to perform the multiple Raman and CL maps outlined in the methods below, as well as because of the unique opportunity to pair these detailed maps with costly, high spatial-resolution secondary ion mass spectrometry (SIMS) measurements. Considering how the mineralogical and isotope measurements from the previous study were correlated with shifts in environmental variables on seasonal timescales (e.g., lake temperature and dissolved oxygen), we expect that these new observations at higher spatial resolution will help to inform the influence (or lack thereof) of organic contents and mineralogy on δ^{18} O-based temperature proxies and to reveal even more ties to environmental conditions on sub-seasonal timescales. Beyond testing their reliability as paleoproxy archives, nacreous pearls also hold historical and contemporary significance in the world of gems and jewelry, contributing approximately 0.5–1 billion dollars (US) per year to the world's economy over the past 30 years (Southgate and Lucas, 2011; van der Schatte Olivier et al., 2020). The genesis of pearls, conditions affecting quality of nacre, and provenance are of interest in gemology. Understanding how pearl nacre is impacted by shifts in climate and local environments is also important for predicting the health of mollusks and the quality of pearls in the future.

88

71

72

73

74

75

76

77

78

79

80

81

82

83

84

85

86

87

2. Materials and Methods

90

91

92

93

94

89

2.1 Samples

The freshwater washboard mussel *Megalonaias nervosa* pearl sample in this study is a cultured (farmed) "keshi" pearl (accidentally cultured by an organic-rich nucleus, instead of an implanted bead nucleus; Fig. 1A, Supplementary Materials, Fig. S1A) that was grown from approximately

1993 to 1996 by the American Pearl Company, TN, USA. The pearl was harvested sometime in late September to early October of 1996, as determined by the 1995–1997 range of harvest dates provided by the American Pearl Company and matching $\delta^{18}O_{Arg}$ measurement patterns with temperature data from the Kentucky Lake Long Term Monitoring Program, Murray State University. This particular pearl is described in detail as "Sample 2" in Farfan et al. (2021). It was selected because it was the most pristine of the three samples measured in that study (it did not contain any obvious inclusions or impurities) and it produced a very clear oxygen isotope record with which to compare the present study. It also has a cylindrical geometry (Fig. 1B, Supplementary Materials, Fig. S1B) that allowed us to more easily compare adjacent transects and maps.

A second, saltwater *Pinctada maxima* keshi pearl (#100515732614 from the Gemological Institute of America) was cultured by Jewelmer in the Philippines (Fig. 1C). Both pearls were embedded in epoxy, sliced in half, and polished such that they could be studied in cross-section.

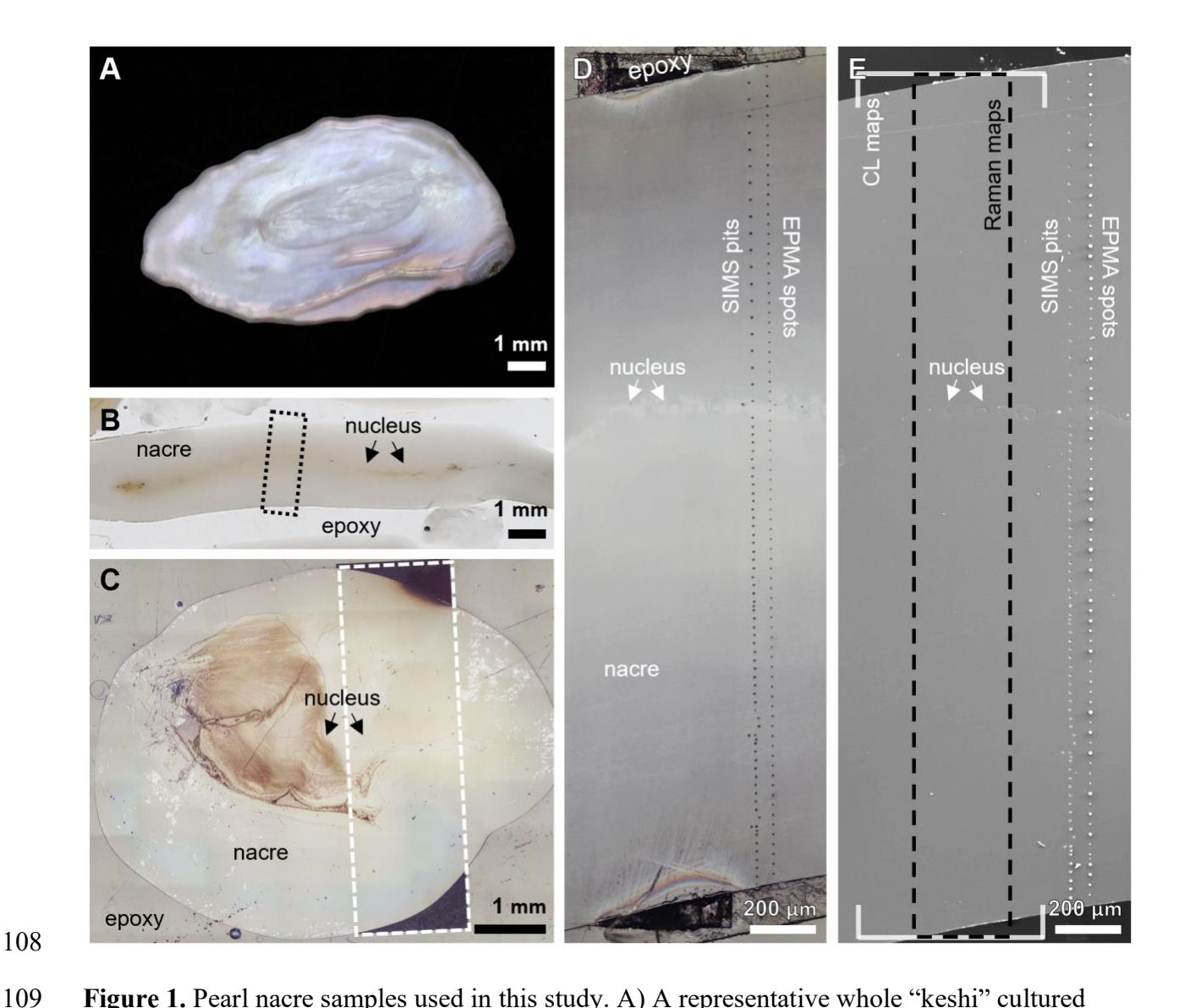


Figure 1. Pearl nacre samples used in this study. A) A representative whole "keshi" cultured pearl showing its pearlescent nacre exterior. B) A photograph of the cross-section of the freshwater pearl examined in this study showing evidence of the organic material that makes up the nucleus. The region mapped in detail in this study is outlined in a dotted black box. C) A photograph of a cross-section of a saltwater pearl examined in this study as a comparison to the freshwater pearl. A white dashed line outlines the area mapped in more detail. D) A composite reflected light photo taken under 20x magnification of the zoomed-in region outlined in black in part B of the freshwater pearl. Transects made by SIMS pits and EPMA spots are labelled. E) A

secondary electron image of the same region of the freshwater shown in part D. Regions mapped by cathodoluminescence (CL) and Raman spectroscopy are outlined in white brackets and a dashed black box, respectively.

2.2 Previous measurements of oxygen isotopes and environmental Kentucky Lake conditions
In Farfan et al. (2021), oxygen isotope data were collected using a CAMECA IMS 1280
Secondary Ion Mass Spectrometer (SIMS) at the WiscSIMS Lab, Department of Geoscience,
University of Wisconsin-Madison. Both $\delta^{18}O_{Arg}$ (oxygen isotope ratios in the nacre aragonite)
and OH/O ratio values were measured along a transect of the freshwater pearl "Sample 2" cross-section. Each SIMS measurement left a ~10 µm pit at ~50 µm intervals (Fig. 1D).

Environmental data for nearby Kentucky Lake, TN, USA were collected by the Kentucky Lake Long-Term Monitoring Program run by Murray State University and are detailed in Farfan et al. (2021). This study on the same freshwater pearl corroborated that $\delta^{18}O_{Arg}$ maxima along the pearl nacre transect matched with winter low temperature conditions in Kentucky Lake, which was used to determine that the pearl grew for four years and accurately captured seasonal environmental conditions across this time period. Kentucky Lake environmental variables captured during this timeframe included temperature, dissolved oxygen, redox potential, total alkalinity, and conductivity.

2.3 Electron Probe Microanalysis (EPMA) and Cathodoluminescence (CL) mapping

Cathodoluminescence (CL) imaging and quantitative chemical analyses were conducted using a JEOL JXA-8530F Field Emission electron probe microanalyzer (EPMA) at the Carnegie Institution for Science, Washington, DC. Data were obtained at 15 kV, 10 nA and a 1 µm beam

diameter, and using the JEOL software. Data were collected using wavelength dispersive spectrometers (WDS), and the elements measured, standards, WDS crystals used, and detection limits, are given in Table S1. Count times were 20 seconds for on-peak measurements and 10 seconds each for lower and upper background measurements, with the exception of the volatile element sodium, for which counting times were 10 seconds (peak) and 5 seconds (upper and lower background). Each analysis took approximately 3 minutes, and the transect along the freshwater pearl totals 83 points at 30 µm spacings. Conditions were set to minimize sample damage, but small damage spots were still visible in the carbonate after analysis (Fig. 1D,E, EPMA spots). Volatile elements such as sodium were measured first. All quantitative element transects across the freshwater pearl are presented in Supplementary Materials, Figure S2 and Table S2.

CL imaging was collected using an Ocean Optics CL system and the xCLent software package at 15 kV and 20 nA with a 1 μ m beam spot size. The CL map was collected in a region adjacent and parallel to the EPMA and SIMS transects along the pearl spanning 2600 \times 550 points at 1 μ m steps and 40 msec dwell time, and took approximately 12 hours to collect (area outlined in Fig. 1E). A CL spectrum from 300 nm to 800 nm wavelengths was collected at each point of the map and intensity maps were created of different regions of the spectrum. A second map using the same collection parameters was run on a saltwater pearl at 2 μ m pixel step size and 20 msec dwell time, spanning 5160 \times 1600 μ m.

Elemental maps were simultaneously collected alongside the CL maps using WDS as described above for P, S, Na, Mg, Mn, and an energy dispersive spectrometer (EDS: a JEOL 30 mm² silicon drift detector) for Ca, P, S, O, Na, Mg, Sr, Ba, Mn, Fe, Al and Zn (Supplementary Materials, Fig. S3). Note that Mg, Fe, Zn, Al, Sr, and Ba are mostly below the detection limit for

the freshwater pearl. Elemental maps for the saltwater pearl can be found in the Supplementary Materials, Figure S4. CL intensities and relative element concentrations integrated from the maps are presented as transects in the Supplementary Materials, Table S3. No sample damage was detected on regions that were mapped. Polished samples were carbon-coated for EPMA analyses and then repolished to thoroughly remove the carbon coat for Raman analyses.

168

169

170

171

172

173

174

175

176

177

178

179

180

181

182

183

184

185

163

164

165

166

167

2.4 Raman spectroscopy

Raman spectroscopy probes the trigonal-planar carbonate group vibrational modes in CaCO₃, offering clues about how the crystal structure of aragonite may shift under different conditions (Urmos et al. 1991; Bischoff et al. 1985). Confocal Raman Spectroscopy was conducted at the Smithsonian National Museum of Natural History in the Department of Mineral Sciences using a Horiba LabRAM Evolution Raman system and a CCD detector. Four Raman maps were collected on the freshwater pearl in order to gather information about the dominant vi symmetric stretching vibrational mode of the carbonate group, the v₄ mode, the translational (T) and librational (L) carbonate group lattice modes, and background luminescence (herein referred to as fluorescence). The Raman mode maps were collected using an unpolarized 785 nm red laser (to avoid background luminescence) coupled with an 1800 grooves/mm grating using a 50x objective with a ~5 μm laser spot size. Raman spectra were collected using full laser power (no neutral density filters) of approximately 13.1 mW. The spectrometer was set at 180 cm⁻¹ to collect the low wavenumber T and L vibrational modes (peaks defined between 140–170 cm⁻¹ and 200–220 cm⁻¹, respectively), at 710 cm⁻¹ to collect the v₄ mode doublet peaks (698–710 cm⁻¹ 1), and at 1070 cm⁻¹ in order to collect the region for the v₁ vibrational mode (peak defined between 1080–1090 cm⁻¹). An additional map was collected using a 532 nm green laser coupled

with a 300 grooves/mm grating, a 50x objective, and 3.2% laser power using neutral density filters (1.7 mW) in order to probe for the background fluorescence emitted by the sample as a potential proxy for organic content. The spectrometer was set at 2200 cm⁻¹ in order to capture the 2400–2700 cm⁻¹ region commonly used to measure background fluorescence (Nehrke and Nouet 2011; Nehrke et al. 2012; Wall and Nehrke 2012; DeCarlo et al. 2018). In this study we also show background fluorescence as a ratio of background fluorescence:v₁ mode peak height using spectra that were background-subtracted using a linear background.

All Raman maps on the freshwater pearl were collected at a 3 μ m-high × 6 μ m-wide pixel resolution of a region that was approximately 300 × 2600 μ m in size and are available in the Supplementary Materials, Figures S5–S8. Each point was collected in duplicate for 2 seconds. Each map took approximately 2.5 days to collect. In order to test reproducibility, a second Raman map of the ν_1 mode was collected along a similar-sized area to the right of the original mapping area, capturing the SIMS and EPMA transects directly (Supplementary Materials, Figs. S9, S11).

In addition to the freshwater pearl maps, the saltwater pearl (Fig. 1C) was mapped for T and L modes at 9 μ m-high \times 15 μ m-wide pixel resolution of a region that was approximately $1600 \times 5200 \ \mu$ m in size and which took 3.5 days to collect. All spectra were processed using LabSpec6 software and were smoothed by 1 point and background-subtracted using a linear background with 256 anchor points. Maps of the processed spectra were created based on peak heights, peak areas, full-width at half-maxima (FWHM), and peak positions of vibrational modes for aragonite. Data from the freshwater pearl Raman maps were then integrated following pearl nacre layers and presented as transects in pearl nacre space (Supplementary Materials, Table S4),

mirroring the EPMA and CL data, as well as former SIMS transects and environmental data from Farfan et al. (2021).

2.5 Statistics

Pearson correlations between all of the variables in this study, as well as selected variables from Farfan et al. 2021, were run using XLSTAT software. Values for coefficients of determination (R^2) and correlation coefficients (R) are presented in the Supplementary Materials, Table S5 for the entire transect, as well as for the whole transect with the nucleus region removed (the region between 900 and 1100 μ m down the transect). In this study, we only discuss relationships and correlations that are statistically significant with p < 0.01. Correlation coefficients between 0.3–0.6 are considered to be "moderate" and over 0.6 are considered to be "strong." R^2 values for all of the variables measured in this study, and select variables from Farfan et al. 2021, are shown as a coefficient diagram in the Supplementary Materials, Figure S10 for the entire freshwater pearl transect, as well as for the transect with the nucleus region removed.

3. Results

3.1 Cathodoluminescence

Cathodoluminescence (CL) imaging records different wavelengths of light emitted by the samples when they are hit with an electron beam, and offers a unique perspective to studying biominerals. Different colors are emitted according to the specific mineral and different

activators or structural defects present, which are commonly associated with specific modes of formation or alteration, such as aragonite formed by biological processes (Barbin, 2000; Toffolo et al. 2019; Toffolo, 2021). Here, we mapped total CL intensity across the pearl transect (Fig. 2A). This approach reveals that the CL signals are highly heterogeneous and follow smooth, fine layer patterns within the pearl, mimicking the layered growth history of the nacre tablets. Overall patterns of CL intensity and colors are mirrored across the pearl nucleus, indicating that these patterns are most likely a result of the nacre growth history and not a random occurrence. The CL signal in this freshwater pearl is dominated by blue and green wavelengths that mix to form an overall teal color, similar to that described in Toffolo et al. 2019 (and green observed in Barbin, 2013). An average spectrum for the entire map is presented in Figure 2B in the estimated teal color (#7FB097). Some regions of the pearl are dominated by strong green wavelengths (outlined as G1 and G2, Fig. 2A), while other regions express a clear presence of blue wavelengths (B1 and B2). Spectra for these specific regions are also presented in Figure 2B with the peak positions for the dominant peaks outlined in their resulting colors (444.4 nm blue and 551.6 nm green). A map representing the region of the spectrum that corresponds to the dominant CL peak at 551.6 nm (Fig. 2C) displays a heterogeneous layer pattern that is very similar to the total CL map (R²=0.98 between CL total and CL 551 nm). A map of the second 444.4 nm CL peak height reveals a different heterogeneous pattern across the pearl transect compared to the 551 nm peak, with wider bands of higher and lower intensities and rough textures throughout (Fig. 2D). Values of CL intensities across the freshwater pearl transect are presented in the Supplementary Materials, Table S3.

231

232

233

234

235

236

237

238

239

240

241

242

243

244

245

246

247

248

249

250

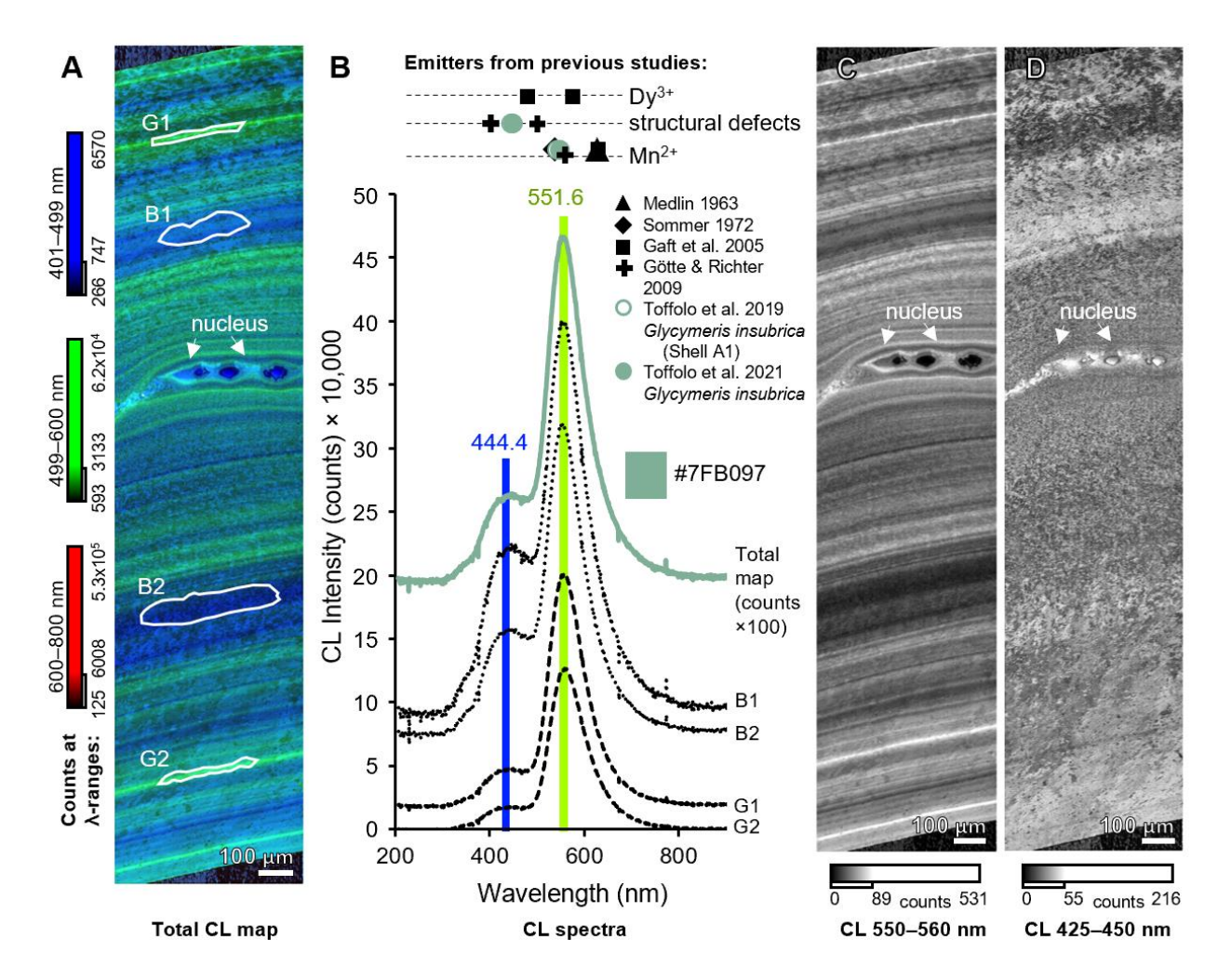


Figure 2. Cathodoluminescence maps and spectra taken on the freshwater pearl. A) A map of total CL counts taken at 1×1 μm pixel step size represented in blue (401–499 nm), green (499–600 nm), and red (600–800 nm) wavelength ranges showing layer features that mirror across the nucleus. Regions outlined in white, "G1" and "G2" represent areas of the map that show strong emission in the green region, while regions "B1" and "B2" represent strong emission in the blue region. B) Representative CL spectra showing an average spectrum for the total CL map in the estimated teal color (#7FB097). Spectra of blue regions 1 and 2 and green regions 1 and 2 are presented in dotted and dashed black lines, respectively. Peak positions for the two peaks are highlighted in the estimated color for that corresponding wavelength (blue for 444.4 nm and green for 551.6 nm). Positions of CL peaks from previous aragonite studies with their associated

emitters are presented above the spectra in this study. C) CL map of counts for the 550–560 nm wavelengths that represent the dominant 551 nm CL peak. D) CL map of counts for the 425–450 nm wavelengths that represents the 444 nm CL peak.

3.2 Raman Spectroscopy

While Raman spectroscopy is typically utilized as a fingerprinting method to identify different mineral phases in pearls, mollusk shells and other biocarbonates (Wehrmeister et al., 2007; 2011; Soldati et al., 2008; Nehrke et al., 2012; Benzerara et al., 2021), here we only observed aragonite and focus on interrogating specific Raman vibrational modes (Fig. 3A; Bischoff et al., 1985; Urmos et al., 1991; Farfan et al., 2021) to determine shifts in the carbonate bonding environment of aragonite across the pearl transects. Showing opposite distributions to the 444 nm CL map (Figs. 2D & 3B), the most striking Raman map across the freshwater pearl cross-section is of the ratio of translational (T):librational (L) peak heights (Fig. 3C). This T:L ratio has been suggested as a way to show relative shifts in tablet orientation as the tablets rotate compared to one another along *a*- and *b*-axes (i.e., Nehrke and Nouet, 2011; Murphy et al., 2021; Farfan et al., 2021).

Visually mimicking the T:L mode ratio map, we observe that the map for the v₁ carbonate symmetric stretching mode full width at half-maximum (FWMH) also shows noticeable shifts across the freshwater pearl transect (Fig. 3D).

Considering that nacre has measurable concentrations of organics known to produce background luminescence signals in Raman spectra (Cuif et al., 2014; DeCarlo et al., 2018), here we measured the background luminescence, herein referred to as background fluorescence, across the pearl transects and observe that the relative intensity of background fluorescence is heterogeneous across the pearl transect with sharp alternating bands of high and low background

fluorescence (Fig. 3E). Normalizing the background fluorescence as a ratio over the dominant v₁ peak height, we observe broad bands of shifting background fluorescence (Fig. 3F).

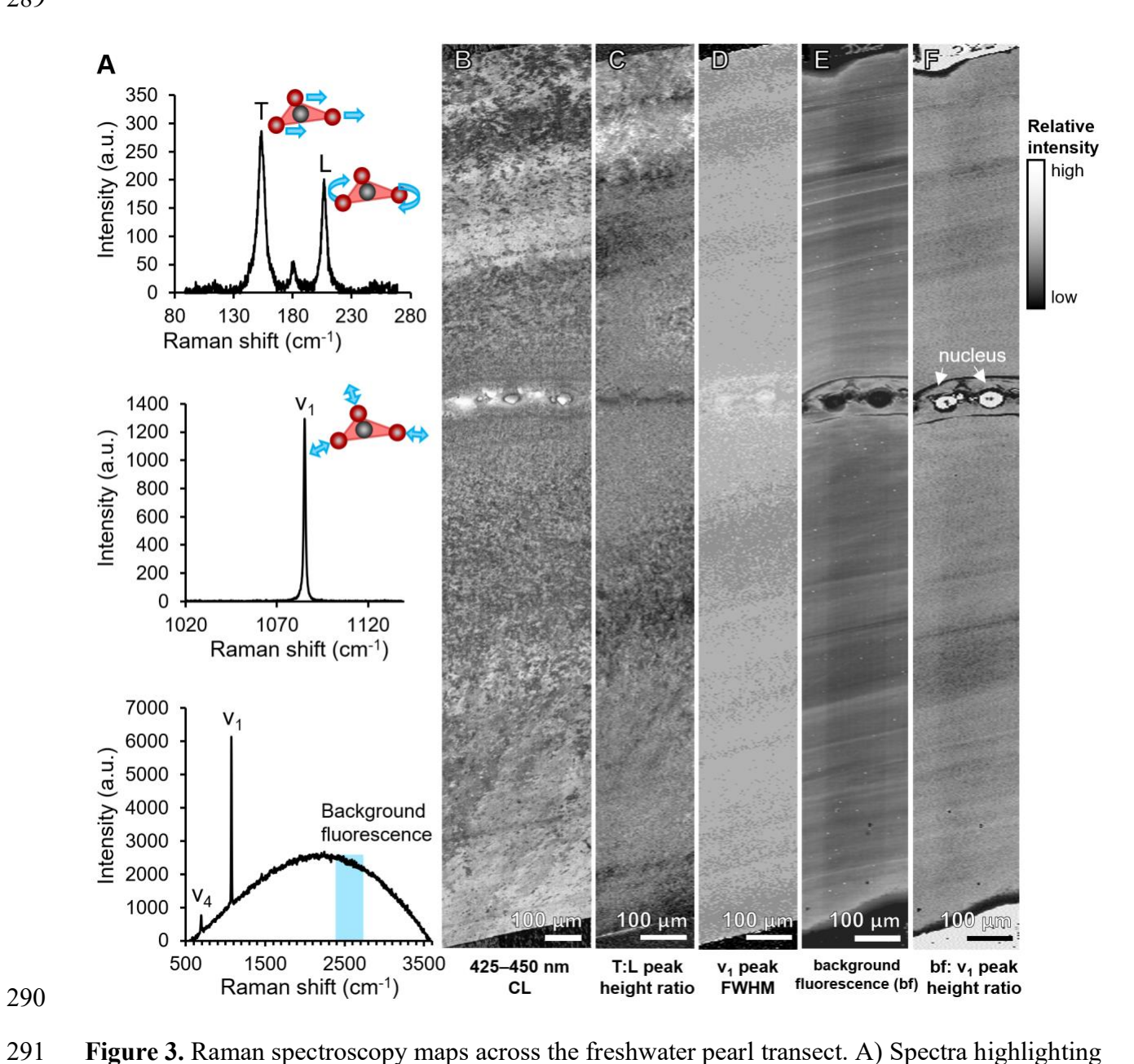


Figure 3. Raman spectroscopy maps across the freshwater pearl transect. A) Spectra highlighting the different Raman vibrational modes of the trigonal-planar carbonate group depicting the translational (T) and librational (L) modes between 130–230 cm⁻¹, the v₁ symmetric stretching

mode (~1090 cm⁻¹), as well as the region between 2300–2700 cm⁻¹ used to estimate the relative contribution of background fluorescence, which also includes the v₄ in-plane bending doublet mode (~700 cm⁻¹) and the v₁ mode. B) The 444 nm CL map from Fig. 2D visually aligned to the Raman maps for comparison. Raman maps collected at 3×6 μm pixel resolution showing C) T:L peak height ratios, D) v₁ mode peak full width at half maximum (FWHM), E) background fluorescence, and F) the ratio of background fluorescence:v₁ mode peak height.

3.3 Element distributions

A combination of quantitative electron probe micro-analysis (EPMA) spot analyses along the transect of the freshwater pearl and accompanying WDS and EDS maps of elemental distributions show that several elements are present in the nacre with heterogeneous distributions above the detection limit (Fig. 4; Supplementary Materials, Figs. S2, S3, Table S2). Trace amounts of manganese (0–0.3 wt%) occur in thin heterogeneous layers observable in the WDS map and EPMA transect (Fig. 4B). Visually, the Mn distribution map resembles the 551 nm CL map (Figs. 2C, 4A). Sulfur and sodium are also present above the detection limit and show heterogeneous layers, but they are not as sharply defined as the Mn layers (Fig. 4C,D).

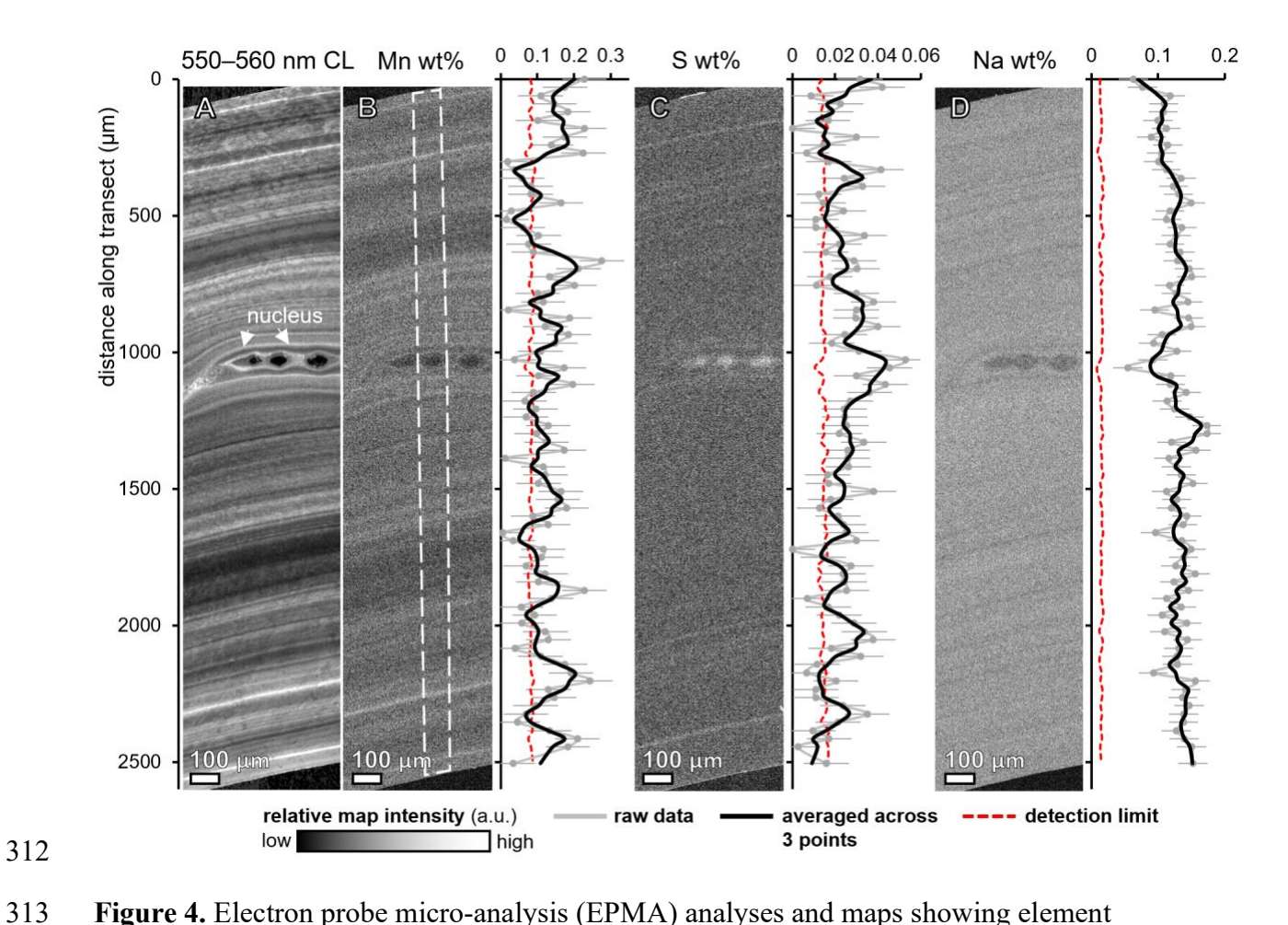


Figure 4. Electron probe micro-analysis (EPMA) analyses and maps showing element distributions and weight percentages across the cross-section map of the freshwater pearl. A) A map of the 551 nm CL signal (550–560 nm range) from Fig. 2C for comparison. B) A wavelength-dispersive X-ray spectroscopy (WDS) map of manganese and accompanying quantitative concentration spot analyses along the transect shown in Figure 1D,E. C) A sulfur WDS map and EPMA transect. D) A sodium WDS map and EPMA transect. Error bars on the

3.4 Alignment with prior work on oxygen isotopes and Kentucky Lake environmental data

EPMA data represent measurement standard errors.

Farfan et al. (2021) demonstrated how nacre aragonite δ^{18} O_{Arg} measurements along the same freshwater pearl sample in this study changes seasonally over the course of four years with temperature and with other environmental conditions recorded by the Kentucky Lake Long Term Monitoring Program (such as dissolved oxygen, total alkalinity, and conductivity as a measure of ionic strength). Integrating our new 551 nm CL map into a linear transect and comparing it with the EPMA transect of Mn wt% (Figs. 2C, 4B, 5A), we observe that they are positively correlated with one another (Fig. 5B, R=0.5, n=83), especially when we compare the 551 nm CL map with the Mn WDS map (Fig. 4B; R=0.66, n=2506). These Mn wt% and 551 nm CL measurements also produce local maxima along the pearl transect on seasonal timescales, like the previous $\delta^{18}O_{Arg}$ and environmental data (Fig. 5A). However, the position of these CL and Mn wt% peak maxima (highlighted in blue bars) are noticeably offset from $\delta^{18}O_{Arg}$ transect peak positions (dashed bright blue lines; Fig. 5A) by approximately 30–200 µm. While there is a chance that this offset is due to an artifact of correlation across the sample from where the SIMS pits were collected compared to where the EPMA transects and CL and Raman maps were collected (Fig. 1E), we believe that this is highly unlikely because the EPMA transect was collected directly adjacent to the SIMS pits. Also, similarly large offsets are not observed when we compare our v₁ mode Raman map to a duplicate Raman map taken directly over the SIMS pits (Supplementary Materials, Fig S11 for detailed explanation). Considering that the 551 nm CL and Mn wt% maxima precede the $\delta^{18}O_{Arg}$ maxima along the pearl growth directions on both sides of the nucleus (Fig. 5), it is likely that they represent the autumn seasons (between August and October) before the cold winter temperatures associated with $\delta^{18}O_{Arg}$ maxima. Beyond these yearly season maxima observations, the high spatial resolution of the 551 nm CL and Mn wt% WDS map data also shows many smaller peaks that record sub-seasonal events. While the

322

323

324

325

326

327

328

329

330

331

332

333

334

335

336

337

338

339

340

341

342

343

Raman background fluorescence:v₁ mode peak height transect integrated from the Raman map (Fig. 3F) does not appear to have distinct local maxima (Fig. 5A), the overall shape of the signal transect positively correlates with the 551 nm CL signal (Fig. 5C, R=0.55, n=805) and the Mn wt% signal (Fig. S12C).

Comparing the 551 nm CL to other physical and environmental variables measured previously in Farfan et al., 2021, we find that the 551 nm CL signal is negatively correlated with nacre tablet thickness and positively correlated with Kentucky Lake conductivity (Fig. 5D) and total alkalinity (Fig. 5E) measurements. Raman background fluorescence:v1 peak height ratios are also negatively correlated with nacre tablet thickness. All plots for correlations described above can be found in the Supplementary Materials, Fig. S12.

Examining the other CL map of the 444 nm signal, we found that this map (Fig. 2D, 3B) is visually similar to the T:L peak height ratio map (Fig. 3C), and that their transects along the pearl are negatively correlated in this study (Supplementary Materials, Fig. S13A,B, R= -0.58, n=836; R=-0.78, n=82 for T:L peak height data from Farfan et al. 2021). The 444 nm CL signal also weakly positively correlates with redox potential (R= 0.39, n=82) and sulfate concentrations (R= 0.38, n=82) in Kentucky Lake water. The v₁ mode peak FWHM transect has visual similarities to the 444 nm CL map and transect (Fig. 3D; Fig. S13A), but we find that it only positively correlates with the sulfur wt% EPMA measurements (Fig. S13C, R=0.52, n= 83).

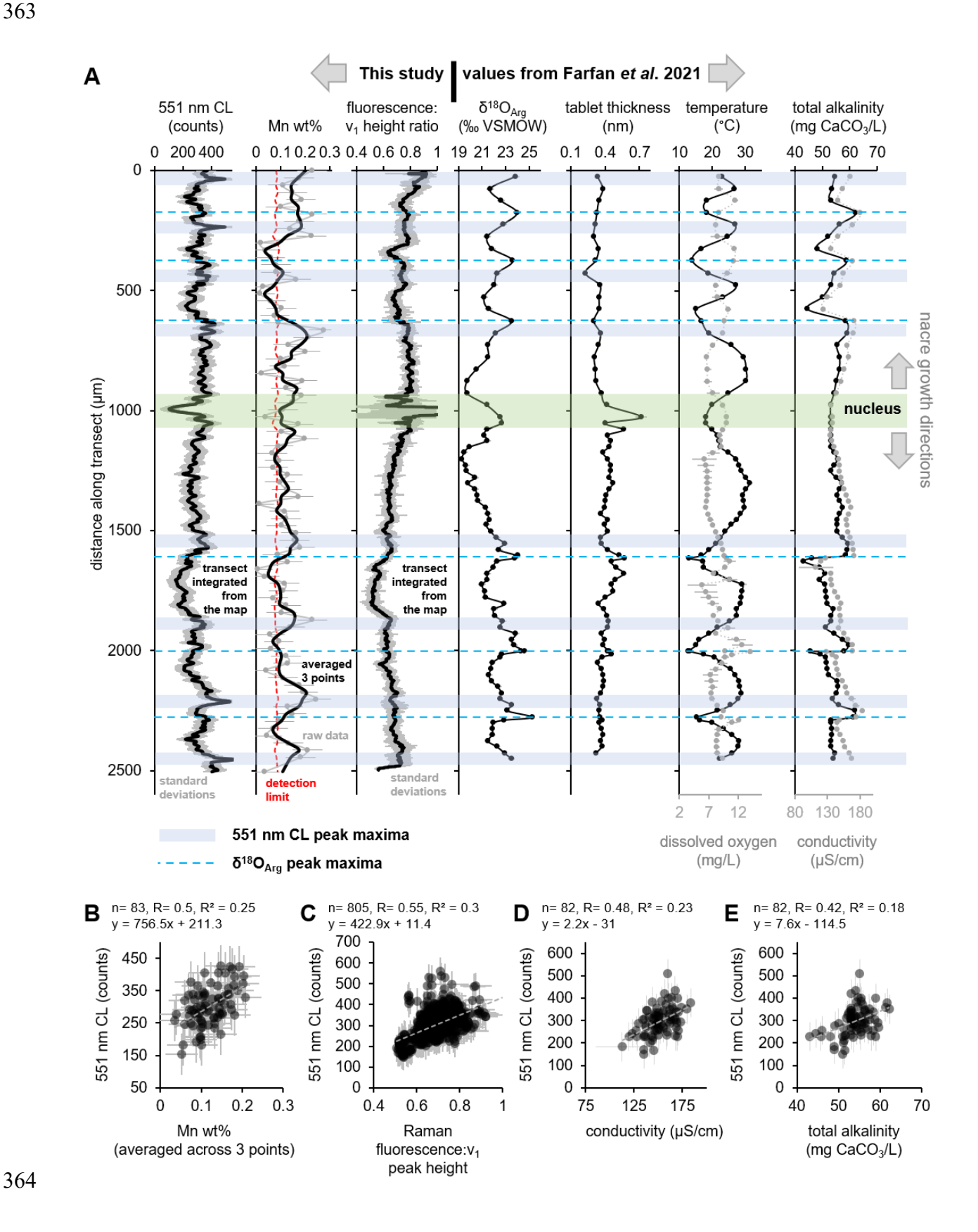


Figure 5. Transects along the freshwater pearl cross-section showing how 551 nm CL, Mn wt%, and Raman background fluorescence:v₁ peak height ratio signals vary over the growth history of the pearl and how they compare to previous nacre δ¹⁸O_{Arg}, nacre tablet thicknesses, and Kentucky Lake environmental measurements by Farfan *et al.* 2021. Error bars represent standard deviations for the CL and Raman maps, standard errors in measurements for Mn wt%, and measurement errors for values from Farfan *et al.* (2021). Pearson correlation plots between 551 nm CL and B) Mn wt% averaged across 3 points, C) Raman fluorescence: v₁ peak height, and Kentucky Lake D) conductivity and E) total alkalinity. Points are shown at 50% transparency. Other correlation plots and details can be found in the Supplementary Materials, Fig. S12.

3.5. Comparison to a saltwater pearl

A saltwater cultured pearl from the Philippines was measured using the same methods as for the freshwater pearl (Figs. 1C and 6). Overall, the sample displays complex zoning around the nucleus in both the optical image (Fig. 6A) and a backscattered electron micrograph (Fig. 6B). Similar to the freshwater pearl, the EDS elemental map of calcium (Fig. 6C) outlines the presence of the pearl versus the surrounding epoxy. Sulfur (Fig. 6D) and sodium (Fig. 6E) WDS maps show relatively homogenous distributions of these elements with lower relative concentrations of sulfur versus sodium. The map of manganese concentrations in the saltwater pearl (Fig. 6F) exhibits very low relative concentrations of Mn, especially compared to the freshwater pearl. For the CL maps, we observe almost no signal for the map of the 551 nm CL signal (Fig. 6G). The 444 nm CL map (Fig. 6H) exhibits very clear growth lines that swirl

around the asymmetrically-shaped nucleus. The Raman spectroscopy T:L peak height ratio map (Fig. 6I) shows similar swirl patterns to the 444 nm CL map, but with inverted intensities.

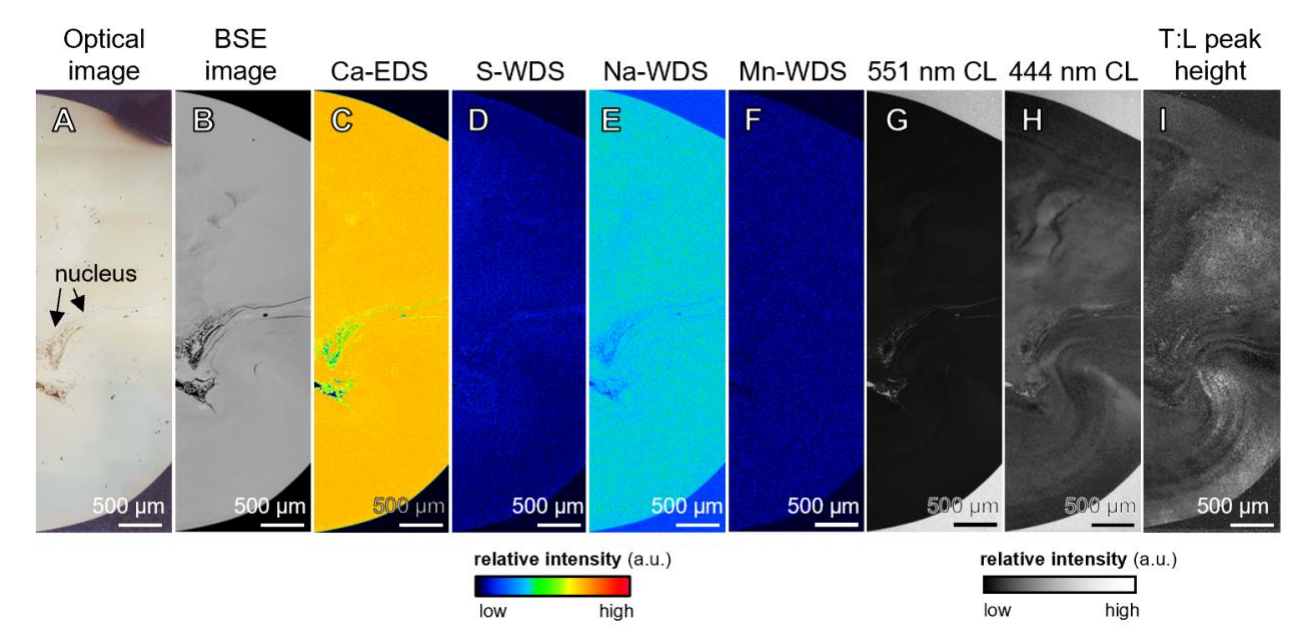


Figure 6. Images and maps of a cross-section of a saltwater pearl from the Philippines depicting A) an optical image of the sample, B) a backscattered electron micrograph, and EDS and WDS maps showing relative concentrations of C) calcium, D) sulfur, E) sodium, and F) manganese. CL counts for G) the major 551 nm CL peak and H) the 444 nm CL peak were collected at 2×2 μm pixel step sizes (beam spot size ≈ 2 μm). I) Raman T:L mode peak height ratios were collected at 9×15 μm pixel resolution (laser spot size ≈5 μm). Scale bars are 500 μm.

4. Discussion

Past studies have demonstrated how the chemical and mineralogical heterogeneity of nacre reflects average (Olson et al., 2012; Gilbert et al., 2017) and seasonal (Farfan et al., 2021) shifts in the environment. In particular, $\delta^{18}O_{Arg}$ in freshwater nacre clearly reflects shifts in lake water $\delta^{18}O$ and lake temperatures across seasonal time scales via bulk and SIMS measurements taken

across shell transects on the millimeter to sub-millimeter scale (Dettman et al., 1999; Pfister et al., 2018). More recently, well-described cultured pearl samples from nearby Kentucky Lake, TN, USA expanded these seasonality observations of coupled δ^{18} O and temperature to include other environmental variables measured in Kentucky Lake (i.e., dissolved oxygen, alkalinity), as well as mineralogical data of the carbonate bonding environment of the aragonite crystal structure shifting across the growth history of the pearls taken on the tens of microns-scale (select previous variables from Farfan et al., 2021 presented in Fig. 5). The present study shows an even higher level of heterogeneity recorded by freshwater pearl nacre on a sub-seasonal scale, observable by CL and Raman mapping at even higher spatial resolutions than has been done via SIMS in the past. In particular, we find that the fine-scale layer features observed via 551 nm CL (Fig. 2C) are most likely linked to manganese distributions (Fig. 4B), while wider 444 nm CL bands (Fig. 2D) across the pearl transect correlate best with shifts in the aragonite crystal morphology and/or structure observed by Raman spectroscopy T:L mode ratios (Fig. 3C).

4.1 Mn distributions preserve lake turnover and rainy seasons in freshwater pearl nacre visible with CL bands

Our results correlating the 551 nm CL map (Fig. 2C) to the quantitative Mn wt% transect and WDS map (Fig. 4B; Fig. 5) suggest that Mn is the most likely driver of the 551 nm CL signal in this freshwater nacre. This is supported by many previous works which suggest that Mn²⁺ is the emitter responsible for the dominant CL signal in biogenic aragonite and calcite (Fig. 2C; Sommer, 1972; Hawkes et al., 1996; Narasimhulu et al., 2000; Götte and Richter, 2009; Toffolo et al, 2019; Toffolo, 2021). In various freshwater shells, Mn is shown to be most likely a combination of mineral-bound Mn²⁺ (substitutions for Ca²⁺ in aragonite and as calcite-structure

micro-domains, as shown by X-ray absorption near edge structure (XANES) spectroscopy) and organically-bound Mn²⁺, although the precise bonding environment is still an active topic of research (Carré et al., 2006; Soldati et al., 2010; 2016; Toffolo, 2021). Quantitative WDS measurements suggest that the average Mn concentration in this pearl is 0.12 ± 0.05 wt% (~1200 ppmw), which falls within the range of Mn concentrations in aragonite that produce strong CL intensities, before self-quenching occurs (>1500 ppm Mn; Götte and Richter, 2009). This freshwater pearl also contains very little iron (68 ppmw), far less than the amount needed for substantial Fe-based CL-quenching (>2000 ppm Fe; Götte and Richter, 2009). In comparison, Götte and Richter (2009) describe a cave flowstone aragonite sample with similar CL peaks broad 440 nm and 520 nm peaks suggested to be inherent to pure aragonite, and a 575 nm peak driven by Mn. They observed that in the aragonite structural signal, the 520 nm peak was 1.5× the height of the 440 nm peak (Götte and Richter, 2009). As the average pearl nacre CL signal in this study shows a 551 nm:444 nm peak ratio of ~2.1, this further suggests that our 551 nm peak has a strong Mn-driven CL signal in addition to any inherent aragonite structural CL signals (Fig. 2B). The Mn²⁺-based CL signal in freshwater nacre is so distinctive that it has even been used to identify the provenance of freshwater pearls from the Mississippi River region, USA versus

427

428

429

430

431

432

433

434

435

436

437

438

439

440

441

442

443

444

445

446

447

448

449

to identify the provenance of freshwater pearls from the Mississippi River region, USA versus those from China (Banerjee and Habermann, 2000). Saltwater abalone *Haliotis rubra* nacre from Port Phillip Bay, Australia has also been shown to produce a green-yellow CL signal when the shells were specifically incubated under highly-elevated Mn concentrations, otherwise the Mn-concentration in typical seawater is too low to be reflected in the aragonite CL (Hawkes et al. 1996). We observed a similar effect when we mapped the CL signals and geochemistry of a cultured pearl grown in seawater and confirmed that the 551 nm CL signal is absent (Fig. 6G) in

this saltwater pearl with little to no Mn (Fig. 6F). In calcitic shells, timed Mn doping has also been applied to shell incubation experiments to measure shell growth rates by imaging the CL bands of the resulting shells (Huyghe et al., 2020).

450

451

452

453

454

455

456

457

458

459

460

461

462

463

464

465

466

467

468

469

470

471

472

As we observe oscillating patterns of high to low Mn concentrations and 551 nm CL signals across the pearl transect that mimic the timeframes for seasonal cycles recorded by $\delta^{18}O_{Arg}$, we assume that these signals are also tied to seasonal changes in the environment. One noticeable difference is that the Mn wt% and 551 nm CL signals are consistently offset from the $\delta^{18}O_{Arg}$ peaks and shifted closer to the nucleus of the pearl (Fig. 5, blue bars), indicating that the environmental conditions driving Mn and 551 nm CL peaks precede the minimum temperature signals of Kentucky Lake recorded as $\delta^{18}O_{Arg}$ maxima (Fig. 5, dashed bright blue lines). This suggests that the Mn and 551 nm CL maxima represent autumn rainy seasons that precede winter. Increased rainfall would lead to more land runoff into Kentucky Lake, which would be rich in Mn from surrounding rocks. This is supported by measurements of Mn concentrations of surface sediments at the Ledbetter Embayment in Kentucky Lake which show that Mn does vary seasonally between "low pool" (113 µg/g dry weight) to "high pool" (241 µg/g dry weight) water stages and that this shift in concentration is likely due to storm water sources that bring the Mn from natural deposits in that region (Seaford et al., 2002). While we do not have a matching precipitation dataset for Kentucky Lake, we did find rainfall records for a weather station in nearby Paris, TN from the National Oceanic and Atmospheric Administration National Centers for Environmental Information (Station USC00406977). These records are highly variable, depending on how they are aligned and averaged across the pearl transect and they do not clearly align with our Mn wt% or 551 nm CL records. However, overall patterns do seem to indicate that rainstorms may precede Mn peaks across the pearl transects (Supplemental Materials, Figure S15). Rainfall with associated land runoff could also explain why the 551 nm CL signal is positively correlated with Kentucky Lake conductivity (a measure of ions in solution) and alkalinity (predominantly carbonate and bicarbonate concentration; Fig. 5; Fig. S11), since both would also be elevated by increased local runoff from sediments during the spring and fall, especially from dissolved carbonates from the Mississippian limestone-shale-coal deposits that the lake sits on (Cobb, 2000).

473

474

475

476

477

478

479

480

481

482

483

484

485

486

487

488

489

490

491

492

493

494

In addition to external sources of manganese from local runoff, manganese is also known to accumulate in bottom waters during periods of lake stratification, such that turnover events in the autumn could also account for increased levels of dissolved manganese in surface waters lasting 6–12 weeks (Howard and Chisholm, 1975). The elevated Mn²⁺ in the lake surface during autumn seasons then gets incorporated into the pearl nacre aragonite, producing the strong CL signal and measurable Mn concentrations in the pearl. Previous studies have also noted that Mn²⁺ concentrations preserve seasonal cycles within shells, however, they have suggested that elevated concentrations occur in summer and that higher organic:mineral shell layers that could potentially make Mn concentrations in shells a useful proxy for primary productivity and Mn concentrations in lakes (Jeffree et al., 1995; Siegele et al., 2001; Soldati et al., 2009). If the Mn concentrations recorded in shells are tied to lake turnover and Mn-rich land runoff from rainfall, freshwater pearl Mn layers may reflect different seasons across the globe, depending on when there is the most rainfall or mixing. Beyond the broad seasonal-scale oscillations in Mn and 551 nm CL, we also observe many thin bands of local maxima between the major maxima (Figs. 2C, 4B, 5) which could be associated with individual, smaller rainstorms. Future studies with lake environmental measurements at higher temporal resolutions may explore the fidelity of CL as a

proxy for lake manganese dynamics (such as Mn oxidation cycles), how nacre captures lake turnover events, and possibly even individual rainstorms at the micron-scale.

497

498

499

500

501

502

503

504

505

506

507

508

509

510

511

512

513

514

515

516

517

495

496

4.2 Seasonal organic signals in freshwater nacre

In addition to being closely correlated with Mn-distributions, we observe that the 551 nm CL signal is moderately correlated with the pearl nacre Raman background fluorescence signal (Fig. 3E), especially when presented as the ratio of background fluorescence: v₁ mode peak height (Figs. 3F, 5C; R=0.55). This background fluorescence signal in biocarbonates is assumed to represent organic compounds, which commonly emit strong fluorescence (Fig. 3A; Cuif et al., 2014; DeCarlo et al., 2018). Thus, we assume that the background fluorescence from other potential abiogenic sources is negligible compared to the organic-driven signal. If this assumption holds, due to the positive correlations between the 551 nm CL signal, Mn distributions, and Raman background fluorescence (Figs. 5, S12), we propose that formation conditions that led to more Mn²⁺ substituted within the aragonite structure also led to elevated organic contents in the nacre, perhaps due to more nutrients and trace elements being available in Kentucky Lake during increased land runoff from autumn and spring rains. To further strengthen this concept, if we assume that the thickness of the organic interlayers remains consistent between nacre tablets of changing sizes, like mortar between bricks (organic interlayers observed by SEM are significantly thinner than the aragonite tablets in Farfan et al., 2021), we would expect regions of nacre with thicker tablets to contain lower organic contents compared to regions with more layers of thinner tablets. This is precisely what we observe, with nacre tablet thickness moderately negatively correlating with the 551 nm CL signal (Fig. S12D; R= -0.44) and the Raman background fluorescence:v₁ mode peak height ratios (Fig. S12E; R= -0.38).

Further observations on the autofluorescence in the freshwater pearl nacre via laser fluorescent microscopy and the preliminary interpretation of these signals are available in the Supplemental Materials, Figures S14 and S16. The specific nature of the organic species leading to the Raman background fluorescence is beyond the scope of this study, but it is well-known that intercrystalline organics such as β -chitin, silk-like proteins, and acidic glycoproteins rich in aspartic acid comprise the organic matrix of mollusk nacres (e.g., Levi-Kalisman et al., 2001). Further studies on how different organic compounds contribute to the background Raman signal and influence isotope measurements would be valuable contributions to this interdisciplinary field of study.

Beyond the influence of organics and manganese on the 551 nm CL signal and fluorescence signals in this freshwater pearl, here we also interrogate how the crystal structure of aragonite changes over the growth history of the pearl. The dissimilar heterogeneous pattern across the pearl transect of the 444 nm CL signal (Fig. 2D) compared to the 551 nm signal (Fig. 2C), indicates that the 444 nm CL signal is likely due to a different CL emitter, such as the "structural defects" attributed to this CL wavelength by previous studies (Götte and Richter, 2009; Toffolo et al., 2019). Here, we corroborate this suggestion that the 444 nm CL signal in bioaragonite is most likely caused by a mineralogical feature by presenting Raman maps of the T:L peak height ratios (Fig. 3C) that mimic the same patterns in the 444 nm CL map (Fig. 2D). The measurement of the T:L peak ratio in nacre has been shown to be a function of nacre tablet orientation as rotations perpendicular to the *c*-axis of the aragonite unit cell (Nehrke and Nouet, 2011; Wall and

Nehrke, 2012; Murphy et al., 2021). We observe the same inverse patterns between the T:L

4.3 Structural shifts across the nacre transect recorded by Raman spectroscopy and CL

mode Raman maps and the 444 nm CL maps in both the freshwater pearl and the saltwater pearl (Fig. 6H,I), further suggesting that the 444 nm CL signal is structural and not due to manganese or some other chemical emitter that differs between the two pearls. Aligning these maps for the freshwater pearl and correlating their values, we observe a moderate to strong negative correlation between 444 nm CL counts and the T:L height ratio (Fig. S13A,B) for both this study (R=-0.58) and for previous T:L height ratios collected at lower spatial resolution (R= -0.78, Farfan et al., 2021).

541

542

543

544

545

546

547

548

549

550

551

552

553

554

555

556

557

558

559

560

561

562

563

Relative tablet orientation has been shown to reflect environmental temperature (Olson and Gilbert, 2012), but beyond this tablet morphology observation, crystallite orientation cannot give us information about structural defects within the aragonite itself. Thus, we turn to changes in Raman peak FWHMs, which are known to widen as a function of more disorder within the crystal structure (DeCarlo et al., 2017). Visually, we observe similar broad patterns across the Raman map of the v₁ mode FWHM (Fig. 3D, Fig. S13A) as we do for the 444 nm CL signal map. The v₁ mode FWHM has been empirically shown to reflect the aragonite saturation state of formation in corals and other aragonites precipitated from saltwater solutions (DeCarlo et al. 2017; Farfan et al. 2022). Comparing the 444 nm CL signal to known environmental measurements in Kentucky Lake, we observe moderate positive correlations with redox potential (R=0.39) and sulfate concentration (R=0.38) in the lake (Fig. S13D,E), however, we are missing aragonite saturation state values for Kentucky Lake in order to properly observe how environmental saturation state may or may not reflect the mussel aragonite saturation state upon aragonite crystal formation. Thus, we suggest that more experimental work be done to establish which environmental variables may influence mineral microstructure and crystallography (and subsequent CL signals) in both freshwater and saltwater nacre. Additionally, we observe that the

transect of sulfur concentrations (Fig. 4C) moderately correlates with the 444 nm CL signal (R= 0.52; Fig. S13C), perhaps adding to the potential relationship we observe with sulfate concentrations in Kentucky Lake (Fig. S13E). Sulfate as SO₄²⁻² is well-known to incorporate into the aragonite structure as a substitute for the carbonate groups (CO₃²⁻²) as "carbonate-associated sulfate" (CAS) in both inorganic and biogenic systems (Pingitore et al., 1995; Farfan et al., 2018; Barkan et al., 2020) which could be a cause of crystallographic disorder in nacre, even in freshwater systems where the sulfate concentrations are much lower than in seawater. Still, it is important to note that the sulfur concentrations in the freshwater pearl from this study fall very close to, or below, the detection limit of the electron microprobe, so this interpretation requires further testing. All of these environmental, structural, and chemical correlations suggest that the Raman T:L ratio (as a proxy for shifts in nacre tablet microstructures) and subsequent 444 nm CL signal are influenced by environmental conditions, and likely those that have an impact on nacre aragonite saturation state and sulfur incorporations.

4.4 Implications for the $\delta^{18}O_{Arg}$ temperature proxy

Secondary ion mass spectrometry (SIMS)-based oxygen isotope $\delta^{18}O$ measurements of carbonates are a novel proxy for tracing past environmental temperatures at the micron-scale, which translates to higher temporal resolutions, compared to traditional bulk analyses (Pfister et al., 2018). These isotope proxies depend on the assumptions that $\delta^{18}O_{Arg}$ measurements faithfully record environmental conditions and are not significantly influenced by mineral crystallography, morphology, geochemistry, or associated organics. To test how robust these assumptions are, we explore how SIMS-based $\delta^{18}O_{Arg}$ and OH/O ratios in this freshwater pearl (SIMS transect

collected at \sim 10 μ m increments and previously published in Farfan et al. 2021, Fig. 1) compared to the organics, structural, and geochemical data in this study.

Previous Raman spectroscopy maps collected under $5\times$ magnification and $30~\mu m$ step sizes revealed that shifts in Raman peak heights across the pearl transect broadly aligned with $\delta^{18}O_{Arg}$ on seasonal timescales (Farfan et al., 2021). Yet, in this study, mapping at higher spatial resolutions with higher-precision measurement parameters, we observe a lack of clear correlations between $\delta^{18}O_{Arg}$ and CL and Raman data, which may indicate that $\delta^{18}O_{Arg}$ values are not strongly affected by Mn concentrations or aragonite carbonate bonding environments observed by these methods at sub-seasonal resolutions in freshwater pearl nacre. This further confirms that $\delta^{18}O_{Arg}$ values do faithfully record lake $\delta^{18}O$ signals that correlate with temperature and dissolved oxygen conditions in Kentucky Lake (Farfan et al., 2021). Consistent offsets between the seasonal nacre-based $\delta^{18}O_{Arg}$ peaks (Fig. 5 light blue dashed lines) that temporally lag behind peaks for the 551 nm CL signal nacre (Fig. 5 highlighted in blue bars) and Mn concentrations also suggest that Mn concentrations in nacre may be shifting before the seasons reach their peak temperatures recorded by the oxygen isotopes and that these signals are decoupled.

5. Conclusions

We show that cathodoluminescence and Raman mapping are powerful tools to observe subseasonal shifts in nacre mineralogy, geochemistry, and organic contents. Our results build on previous studies that suggest that the dominant 551 nm CL signal in a freshwater pearl is most likely due to Mn²⁺ substituted within the aragonite structure, as evidenced by qualitative Mn

maps and quantitative Mn wt% measurements that show close correlations with the 551 nm CL signal. This is further confirmed by comparing our freshwater pearl to a saltwater pearl that displays a lack of 551 nm CL signal and low-Mn content. By combining CL with Raman spectroscopy, we are able to show that the 551 nm CL signal is also correlated with Raman background fluorescence typically associated with organics. Both organics and Mn concentrations in the pearls are likely influenced by spring and autumn lake turnover mixing events and rainstorms with land runoff that elevate manganese and nutrients in Kentucky Lake. In contrast, the secondary 444 nm CL peak signal displays a distinct heterogeneous pattern across the pearl transect that does not match the seasonal 551 nm CL signal and instead is correlated with aragonite crystallographic shifts, as evidenced by the Raman-based T:L ratio (a measure of tablet orientation), as well as with environmental data from Kentucky Lake for sulfate and redox potential. It is possible that carbonate-associated sulfate may play a role in the crystallographic distortions in aragonite that lead to this 444 nm CL signal, but this should be explored more carefully in future studies. Overall, there are no clear correlations between $\delta^{18}O_{Arg}$ measurements and CL signals or Raman data that would indicate that organics and aragonite crystallography play an influencing role in shifting $\delta^{18}O_{Arg}$, suggesting that nacre faithfully records environmental δ^{18} O_{water} values. To compare to our case study of this freshwater pearl, we suggest that future experiments are needed to further target the roles of specific environmental variables (such as aragonite saturation state and manganese and sulfate concentrations in solution) on structural and geochemical signals visible by CL and Raman spectroscopy. Now that we have established that the Raman T:L ratio and v₁ mode maps are the most informative in this very well-described freshwater pearl sample (and a saltwater pearl counterpart), future studies

610

611

612

613

614

615

616

617

618

619

620

621

622

623

624

625

626

627

628

629

630

may target these specific Raman modes and CL 551 nm and 444 nm signals as high-resolution transects (as opposed to full maps) to save time and extend these observations to more samples.

Acknowledgements

We thank Rob Wardell for helping with Raman spectroscopy in the NMNH Department of Mineral Science, Tim Gooding for help with sample preparation in the NMNH Department of Mineral Sciences, and Scott Whitaker for help using the fluorescence microscope at the Smithsonian NMNH LAB. This research was supported by the Coralyn Whitney Curator Endowment. WiscSIMS is supported by NSF (EAR-2004618) and the University of Wisconsin-Madison.

Appendix A. Supplementary Material

Figures S1–S16 show photos of the freshwater keshi pearls, elemental maps (EDS and WDS) collected by EPMA, all of the Raman maps, a matrix of coefficients of determination for all of the variables in the study, an example of a duplicate Raman map data, correlation plots between various important potential relationships between the many variables, a comparison of the pearl transects to rainfall data and Farfan *et al.* 2021 data, and fluorescence microscopy images. Tables S1–S5 present the set-up for the EPMA analyses (such as the standards used), EPMA data, CL and trace element transect data, Raman spectroscopy map data, and Pearson correlations between all of the variables presented in this work. Finally, we also include a more in-depth discussion on organics in the freshwater pearl nacre.

References Addadi, L., Weiner, S. 1997. A pavement of pearl. Nature. 389(6654), 912–913. Addadi, L., Joester, D., Nudelman, F., Weiner, S. 2006. Mollusk shell formation: a source of new concepts for understanding biomineralization processes. Eur. J. Chem. 12(4), 980–987. Banerjee, A., Habermann, D. 2000. Identification of Chinese fresh-water pearls using Mn²⁺ activated cathodoluminescence. Carbonates Evaporites 15(2), 138–148. Barbin, V. 2000. Cathodoluminescence of carbonate shells: biochemical vs diagenetic process. In Cathodoluminescence in Geosciences, Springer, Berlin, Heidelberg, pp 303–329. Barbin, V. 2013. Application of cathodoluminescence microscopy to recent and past biological materials: a decade of progress. Mineral. Petrol. 107(3), 353–362. Barkan, Y., Paris, G., Webb, S. M., Adkins, J. F., Halevy, I. 2020. Sulfur isotope fractionation between aqueous and carbonate-associated sulfate in abiotic calcite and aragonite. Geochim. Cosmochim. Acta 280, 317–339. Barthelat, F., Yin, Z., Buehler, M. J. 2016. Structure and mechanics of interfaces in biological materials. Nat. Rev. Mater. 1, 1–16.

- Benzerara, K., Bolzoni, R., Monteil, C., Beyssac, O., Forni, O., Alonso, B., Asta, M.P., Lefevre,
- 679 C. 2021. The gammaproteobacterium Achromatium forms intracellular amorphous calcium
- carbonate and not (crystalline) calcite. *Geobiology*. 19(2), 199–213.

681

- Bischoff, W. D., Sharma, S. K., MacKenzie, F. T. 1985. Carbonate ion disorder in synthetic and
- biogenic magnesian calcites: A Raman spectral study. Am. Min. 70(5–6), 581–589.

684

- 685 Carré, M., Bentaleb, I., Bruguier, O., Ordinola, E., Barrett, N. T., Fontugne, M. 2006.
- 686 Calcification rate influence on trace element concentrations in aragonitic bivalve shells:
- evidences and mechanisms. Geochim. Cosmochim. Acta 70(19), 4906–4920.

688

- 689 Cobb, J.C. 2000. Geologic Map of Kentucky, Kentucky Geological Survey,
- 690 http://www.uky.edu/KGS/pdf/mc20 12.pdf

691

- 692 Cuif, J. P., Burghammer, M., Chamard, V., Dauphin, Y., Godard, P., Le Moullac, G., Nehrke,
- 693 G., Perez-Huerta, A. 2014. Evidence of a biological control over origin, growth and end of the
- 694 calcite prisms in the shells of *Pinctada margaritifera* (Pelecypod, Pterioidea). Minerals 4(4),
- 695 815-834.

696

- DeCarlo, T. M., D'Olivo, J. P., Foster, T., Holcomb, M., Becker, T., McCulloch, M. T. 2017.
- 698 Coral calcifying fluid aragonite saturation states derived from Raman spectroscopy.
- 699 Biogeosciences 14(22), 5253–5269.

- 701 DeCarlo, T. M., Ren, H., Farfan, G. A. 2018. The origin and role of organic matrix in coral
- 702 calcification: insights from comparing coral skeleton and abiogenic aragonite. Front. Mar. Sci. 5,
- 703 170.

704

- Espinosa, H. D., Juster, A. L., Latourte, F. J., Loh, O. Y., Gregoire, D., Zavattieri, P. D. 2011.
- Tablet-level origin of toughening in abalone shells and translation to synthetic composite
- materials. Nat. Commun. 2, 173. 1 p only?

708

- 709 Dettman, D. L., Reische, A. K., Lohmann, K. C. 1999. Controls on the stable isotope
- 710 composition of seasonal growth bands in aragonitic fresh-water bivalves (Unionidae). Geochim.
- 711 Cosmochim. Acta. 63(7–8), 1049–1057.

712

- Farfan, G. A., Apprill, A., Webb, S. M., Hansel, C. M. 2018. Coupled X-ray fluorescence and X-
- ray absorption spectroscopy for microscale imaging and identification of sulfur species within
- 715 tissues and skeletons of scleractinian corals. Anal. Chem. 90(21), 12559–12566.

716

- Farfan, G. A., Zhou, C., Valley, J. W., Orland, I. J. 2021. Coupling mineralogy and oxygen
- isotopes to seasonal environmental shifts recorded in modern freshwater pearl nacre from
- Kentucky Lake. Geochem. Geophys. Geosystems 22(12), e2021GC009995.

- Farfan, G. A., Apprill, A., Cohen, A., DeCarlo, T. M., Post, J. E., Waller, R. G., and Hansel, C.
- M. 2022. Crystallographic and chemical signatures in coral skeletal aragonite. Coral Reefs 41(1),
- 723 19–34.

- 724
- Gilbert, P. U. P. A., Abrecht, M., Frazer, B. H. 2005. The organic-mineral interface in
- biominerals. Reviews in Mineralogy and Geochemistry, 59(1), 157–185.
- 727
- Gilbert, P. U. P. A., Bergmann, K. D., Myers, C. E., Marcus, M. A., DeVol, R. T., Sun, C. Y.,
- 729 Blonsky, A.Z., Tamre, E., Zhao, J., Karan, E. A., Tamura, N., Tamurag, N., Lemere, S., Giuffre,
- A. J., Giribete, G., Eiler, J. M., Knoll, A. H. 2017. Nacre tablet thickness records formation
- temperature in modern and fossil shells. Earth and Planet. Sci. Lett. 460, 281–292.
- 732
- Gim, J., Schnitzer, N., Otter, L.M., Cui, Y., Motreuil, S., Marin, F., Wolf, S.E., Jacob, D.E.,
- Misra, A., Hovden, R. 2019. Nanoscale deformation mechanics reveal resilience in nacre of
- 735 *Pinna nobilis* shell. Nat. Commun. 10(1), 1–8.
- 736
- Gim, J., Koch, A., Otter, L.M., Savitzky, B.H., Erland, S., Estroff, L.A., Jacob, D.E., Hovden, R.
- 738 2021. The mesoscale order of nacreous pearls. Proc. Natl. Acad. Sci. U.S.A. 118(42),
- 739 p.e2107477118
- 740
- Götte, T., Richter, D.K. 2009. Quantitative aspects of Mn-activated cathodoluminescence of
- natural and synthetic aragonite. Sedimentology 56(2), 483–492.
- 743
- Hawkes, G. P., Day, R. W., Wallace, M. W., Nugent, K. W., Bettiol, A. A., Jamieson, D. N.,
- 745 Williams, M. C. 1996. Analyzing the growth and form of mollusc shell layers, in situ, by
- cathodoluminescence microscopy and Raman spectroscopy. J. Shellfish Res. 15(3), 659–666.

747

- Howard, H. H., Chisholm, S. W. 1975. Seasonal variation of manganese in a eutrophic lake. Am.
- 749 Midl. Nat. 188–197.

750

- Huyghe, D., Emmanuel, L., de Rafélis, M., Renard, M., Ropert, M., Labourdette, N., Lartaud, F.
- 752 2020. Oxygen isotope disequilibrium in the juvenile portion of oyster shells biases seawater
- temperature reconstructions. Estuar. Coast. Shelf Sci. 240, 106777.

754

- Jeffree, R. A., Markich, S. J., Lefebvre, F., Thellier, M., Ripoll, C. 1995. Shell microlaminations
- of the freshwater bivalve *Hyridella depressa* as an archival monitor of manganese water
- concentration: experimental investigation by depth profiling using secondary ion mass
- 758 spectrometry (SIMS). Experientia 51(8), 838–848.

759

- Levi-Kalisman, Y., Falini, G., Addadi, L., Weiner, S. 2001. Structure of the nacreous organic
- matrix of a bivalve mollusk shell examined in the hydrated state using cryo-TEM. J. Struct. Biol.
- 762 135(1), 8–17.

763

- Linzmeier, B. J., Landman, N. H., Peters, S. E., Kozdon, R., Kitajima, K., Valley, J. W. 2018.
- 765 Ion microprobe stable isotope evidence for ammonite habitat and life mode during early
- ontogeny. Paleobiology 44(4), 1–25.

767

- Murphy, A. E., Jakubek, R. S., Steele, A., Fries, M. D., Glamoclija, M. 2021. Raman
- spectroscopy provides insight into carbonate rock fabric based on calcite and dolomite crystal
- 770 orientation. J. Raman Spectrosc. 52(6), 1155–1166.

771

- Narasimhulu, K. V., Rao, J. L. 2000. EPR and IR spectral studies of the sea water mussel *Mytilus*
- 773 conradinus shells. Spectrochim. Acta A Mol. Biomol. Spectrosc. 56(7), 1345–1353.

774

- Nehrke, G., Nouet, J. 2011. Confocal Raman microscope mapping as a tool to describe different
- mineral and organic phases at high spatial resolution within marine biogenic carbonates: case
- study on *Nerita undata* (Gastropoda, Neritopsina). Biogeosciences 8(12), 3761–3769.

778

- Nehrke, G., Poigner, H., Wilhelms-Dick, D., Brey, T., Abele, D. 2012. Coexistence of three
- 780 calcium carbonate polymorphs in the shell of the Antarctic clam *Laternula elliptica*. Geochem.
- 781 Geophys. Geosystems 13(5).

782

- Olson, I. C., Gilbert, P. U. P. A. 2012. Aragonite crystal orientation in mollusk shell nacre may
- depend on temperature. The angle spread of crystalline aragonite tablets records the water
- temperature at which nacre was deposited by *Pinctada margaritifera*. Faraday Discuss. 159(1),
- 786 421–432.

787

- Olson, I. C., Kozdon, R., Valley, J. W., Gilbert, P. U. P. A. 2012. Mollusk shell nacre
- villa villa
- 790 134(17), 7351–7358.

791

- Pfister, L., Thielen, F., Deloule, E., Valle, N., Lentzen, E., Grave, C., Beisel, J.N., McDonnell,
- J.J. 2018. Freshwater pearl mussels as a stream water stable isotope recorder. Ecohydrology
- 794 11(7), e2007.

795

- Pingitore Jr, N. E., Meitzner, G., Love, K. M. 1995. Identification of sulfate in natural carbonates
- by X-ray absorption spectroscopy. Geochim. Cosmochim. Acta 59(12), 2477–2483.

798

- Rousseau, M., Rollion-Bard, C. 2012. Influence of the depth on the shape and thickness of nacre
- tablets of *Pinctada margaritifera* pearl oyster, and on oxygen isotopic composition. Minerals
- 801 2(1), 55–64.

802

- 803 Seaford, K. D., Loganathan, B. G., Owen, D. A. 2002. Effect of water level fluctuations on
- 804 selected organic compounds and metal concentrations in surface sediments from Ledbetter
- Embayment of Kentucky Lake. J. Environ. Monit. Restoration 1, 64–79.

806

- Siegele, R., Orlic, I., Cohen, D. D., Markich, S. J., Jeffree, R. A. 2001. Manganese profiles in
- freshwater mussel shells. Nucl. Instrum. Methods Phys. Res. B: Beam Interact. Mater. At.
- 809 181(1–4), 593–597.

810

- 811 Soldati, A. L., Jacob, D. E., Wehrmeister, U., Häger, T., Hofmeister, W. 2008. Micro-Raman
- spectroscopy of pigments contained in different calcium carbonate polymorphs from freshwater
- cultured pearls. J. Raman Spectrosc. 39(4), 525–536.

Soldati, A. L., Jacob, D. E., Schöne, B. R., Bianchi, M. M., Hajduk, A. 2009. Seasonal periodicity of growth and composition in valves of *Diplodon chilensis patagonicus* (d'Orbigny, 1835). J. Molluscan Stud. 75(1), 75–85. Soldati, A. L., Goettlicher, J., Jacob, D. E., Vilas, V. V. 2010. Manganese speciation in *Diplodon* chilensis patagonicus shells: a XANES study. J. Synchrotron Radiat. 17(2), 193–201. Soldati, A. L., Jacob, D. E., Glatzel, P., Swarbrick, J. C., Geck, J. 2016. Element substitution by living organisms: the case of manganese in mollusc shell aragonite. Sci. Rep. 6(1), 1–9. Sommer, S. E. 1972. Cathodoluminescence of carbonates, 1. Characterization of cathodoluminescence from carbonate solid solutions. Chem. Geol. 9(1–4), 257–273. Southgate, P., Lucas, J. (Eds.). 2011. The pearl oyster. Elsevier. Thompson, D. M. 2022. Environmental records from coral skeletons: A decade of novel insights and innovation. Wiley Interdiscip. Rev. Clim. Change 13(1), e745. Toffolo, M. B., Ricci, G., Caneve, L., Kaplan-Ashiri, I. 2019. Luminescence reveals variations in local structural order of calcium carbonate polymorphs formed by different mechanisms. Sci.

Rep. 9(1), 1–15

837 Toffolo, M. B. 2021. The significance of aragonite in the interpretation of the microscopic 838 archaeological record. Geoarchaeology, 36(1), 149–169. 839 840 Urmos, J., Sharma, S. K., Mackenzie, F. T. 1991. Characterization of some biogenic carbonates 841 with Raman spectroscopy. Am. Min. 76(3-4), 641-646. 842 843 van der Schatte Olivier, A., Jones, L., Vay, L. L., Christie, M., Wilson, J., Malham, S. K. 2020. 844 A global review of the ecosystem services provided by bivalve aquaculture. Rev. Aquac. 12(1), 845 3–25. 846 847 Wall, M., Nehrke, G. 2012. Reconstructing skeletal fiber arrangement and growth mode in the 848 coral Porites lutea (Cnidaria, Scleractinia): a confocal Raman microscopy study. Biogeosciences 849 9(11), 4885–4895. 850 851 Wehrmeister, U., Jacob, D. E., Soldati, A. L., Häger, T., Hofmeister, W. 2007. Vaterite in 852 freshwater cultured pearls from China and Japan. J. Gemmol. 30(7/8), 399. 853 854 Wehrmeister, U., Jacob, D.E., Soldati, A.L., Loges, N., Häger, T., Hofmeister, W. 2011. 855 Amorphous, nanocrystalline and crystalline calcium carbonates in biological materials. J. Raman

856

857

Spectrosc. 42(5), 926–935.

Supplementary Materials

Geochemical and mineralogical proxies beyond temperature: fall seasons trapped in freshwater nacre

Gabriela A. Farfan¹, Emma S. Bullock², Chunhui Zhou³, John W. Valley⁴

¹Department of Mineral Sciences, National Museum of Natural History, Smithsonian Institution, Washington, DC, 20560

²Earth and Planets Laboratory, Carnegie Institution for Science, Washington, DC, 20015

³Gemological Institute of America, New York, NY 10036

⁴Department of Geoscience, University of Wisconsin, Madison, WI 53706

TABLE OF CONTENTS

Figures:

Figure S1. Photos of freshwater "keshi" pearls.

Figure S2. Trace element wt% values across the pearl transect by wavelength-dispersive X-ray spectrometry (WDS) collected with EPMA.

Figure S3. Elemental maps of the freshwater pearl via WDS and EDS collected with EPMA

Figure S4. Elemental maps of the saltwater pearl via WDS and EDS collected with EPMA

Figure S5. Raman maps of T and L modes

Figure S6. Raman maps of the v4 mode

Figure S7. Raman maps of the v_1 mode

Figure S8. Raman maps of background luminescence (fluorescence)

Figure S9. Duplicate Raman maps of the v_1 mode on an adjacent area over the SIMS pits and EPMA spots

Figure S10. Coefficients of determination (R²) matrix of most variables in this study

Figure S11. Comparing alignment offsets between Raman maps on two adjacent regions

Figure S12. Correlation plots between 551 nm CL and other variables in this study and Farfan *et al.*, 2021

Figure S13. Transects that resemble the 444 nm CL signal and associated correlation plots

Figure S14. Correlation plots between potential organic-related materials and the variables in this study

Figure S15. Rainfall records for nearby Paris, TN compared to our 551 nm CL and Mn concentration data

Figure S16. Fluorescent microscopy images

A discussion of organics in freshwater pearl nacre—Raman background fluorescence, laser autofluorescence, and OH contents

Table S1. Measurement details and standards for the wavelength-dispersive (WDS) analysis on the electron microprobe.

Tables included in separate Excel spreadsheets:

Table S2. (Presented as a separate Excel spreadsheet). Quantitative EPMA analyses of trace elements across the freshwater pearl at 30-μm increments.

Table S3. (Presented as a separate Excel spreadsheet). CL and trace element transects integrated from the electron microprobe maps (Figs. 2,4).

Table S4. (Presented as a separate Excel spreadsheet). Raman intensities, FWHMs, or ratios for all modes measured in this study based on maps (Figs. 3, S4–S8) integrated following pearl nacre layers and presented as transects in pearl nacre space at 3-μm increments.

Table S5. (Presented as a separate Excel spreadsheet). Pearson correlation results between all variables in this study listed as coefficients of determination (R^2) and correlation coefficients (R).

FIGURES

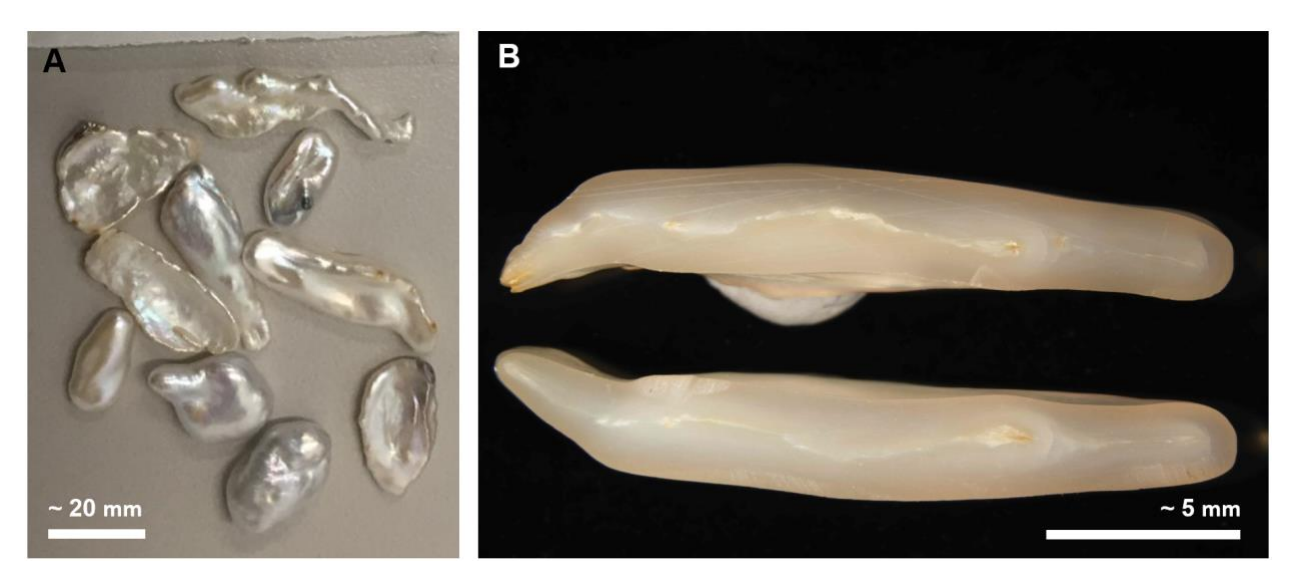


Figure S1. A) Freshwater cultured "keshi" pearls from the batch that "Sample 2" in this study was harvested from (harvested between 1994–1996). B) The freshwater pearl in this study sliced in half, showing a thin line along the middle that is the organic nucleus.

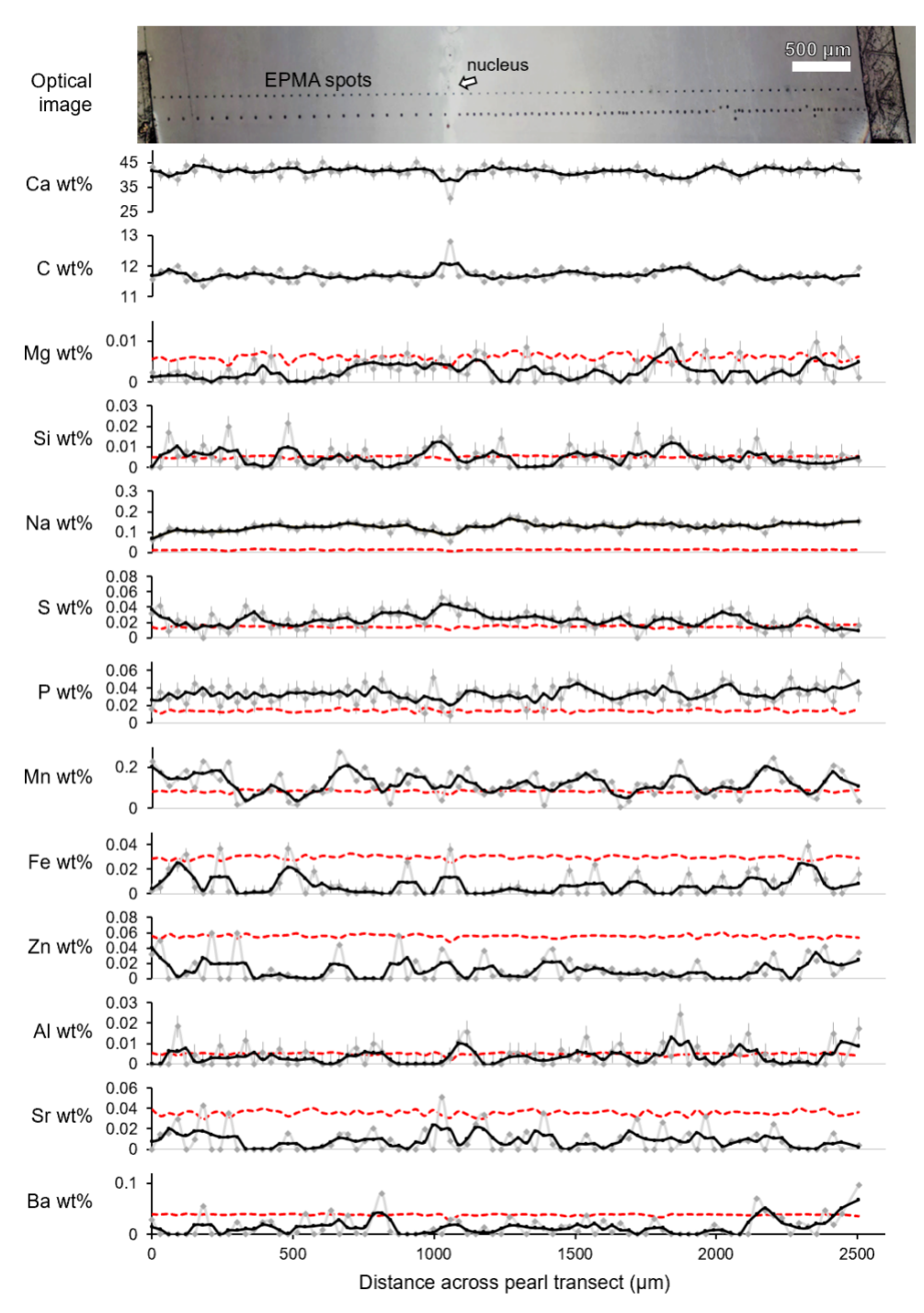


Figure S2. Quantitative geochemical measurements across the freshwater pearl transect via standardized wavelength-dispersive X-ray spectrometry (WDS) analyses by EPMA taken at 30-μm increments. The optical image of the pearl transect is presented at the top, followed by the transects for each element. Raw data are presented as grey points connected by grey lines, the black lines represent data smoothed by averaging across three points, and the red-dashed lines are the analytical detection limits for each element that has wt% values that fall close or below these limits. Error bars represent the standard errors in measurements. Standards are listed in Table S1 and all data are presented in Table S2.

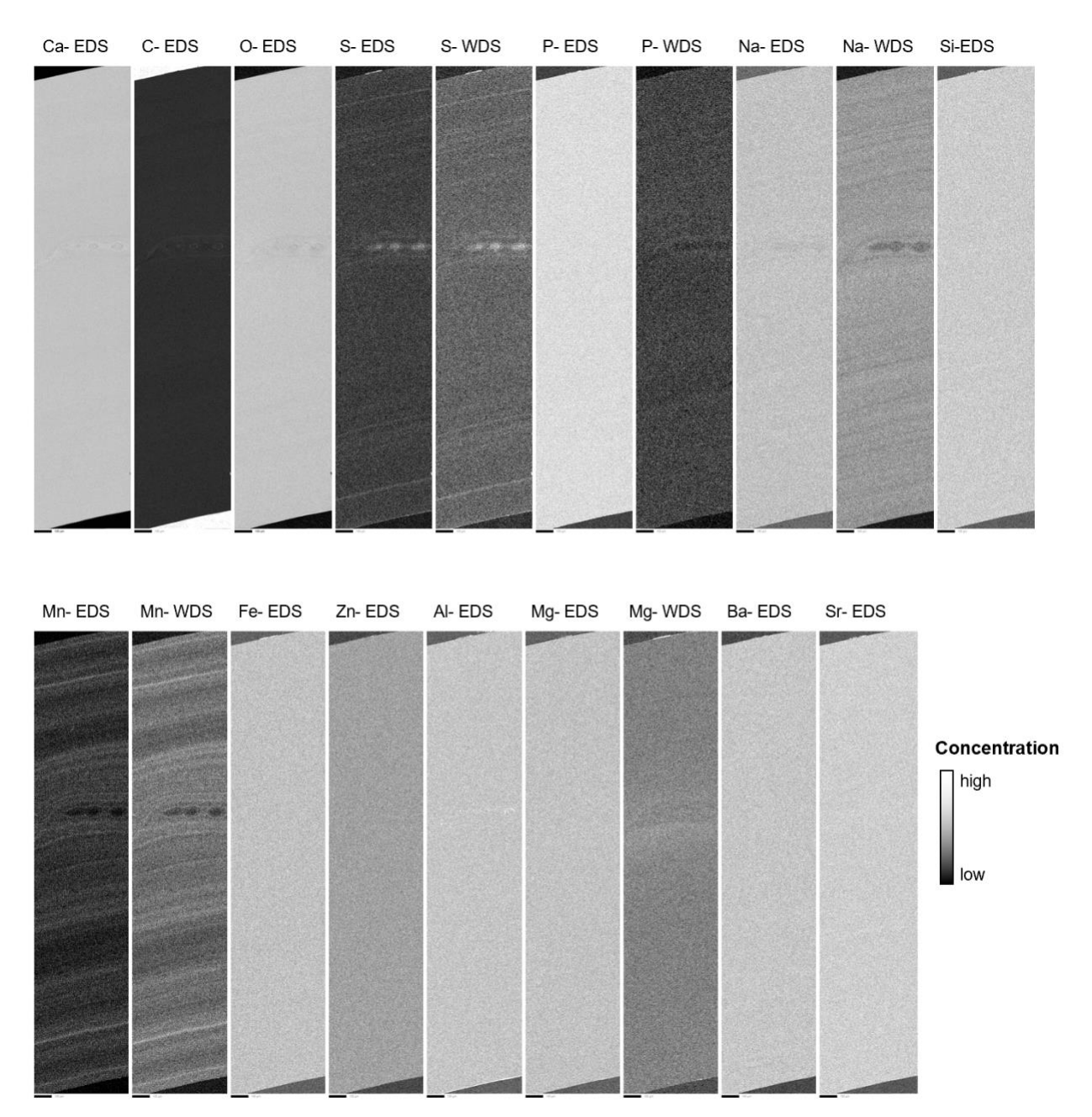


Figure S3. Elemental maps of relative element concentrations across the freshwater pearl transect using wavelength-dispersive X-ray spectrometry (WDS), and energy dispersive X-ray spectrometry (EDS) at 1 μ m pixel step sizes with a beam spot size of ~1 μ m, which yields an effective spatial resolution of approximately 2.5 μ m, dependent on the density of aragonite. The black scale bars are 100 μ m.

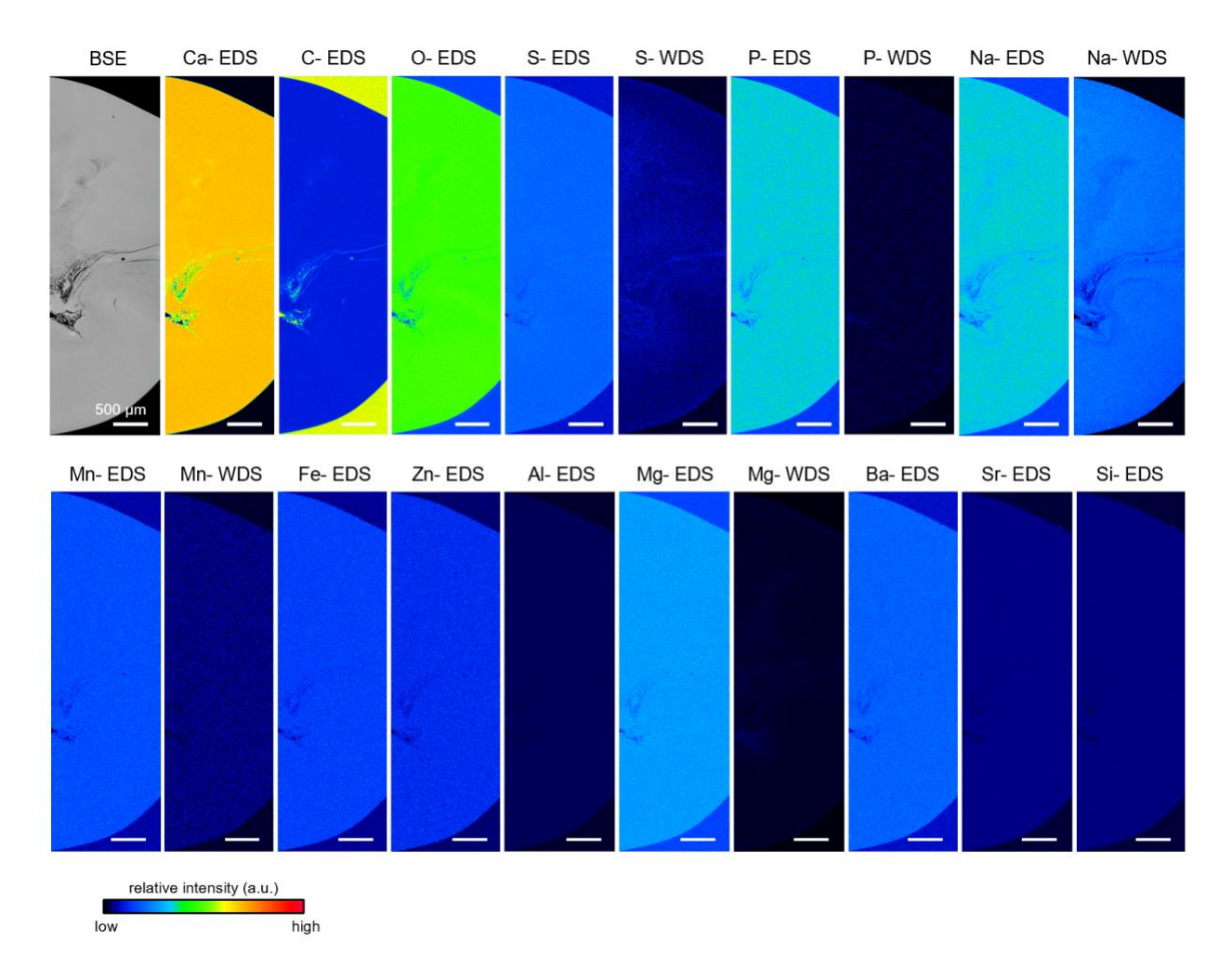


Figure S4. Elemental maps of a saltwater pearl using wavelength-dispersive X-ray spectrometry (WDS), and energy dispersive X-ray spectrometry (EDS) at 2 μ m step sizes. The white scale bars are 500 μ m. Note that the center nucleus of the pearl (as seen in BSE) is dark due to epoxy filling in holes.

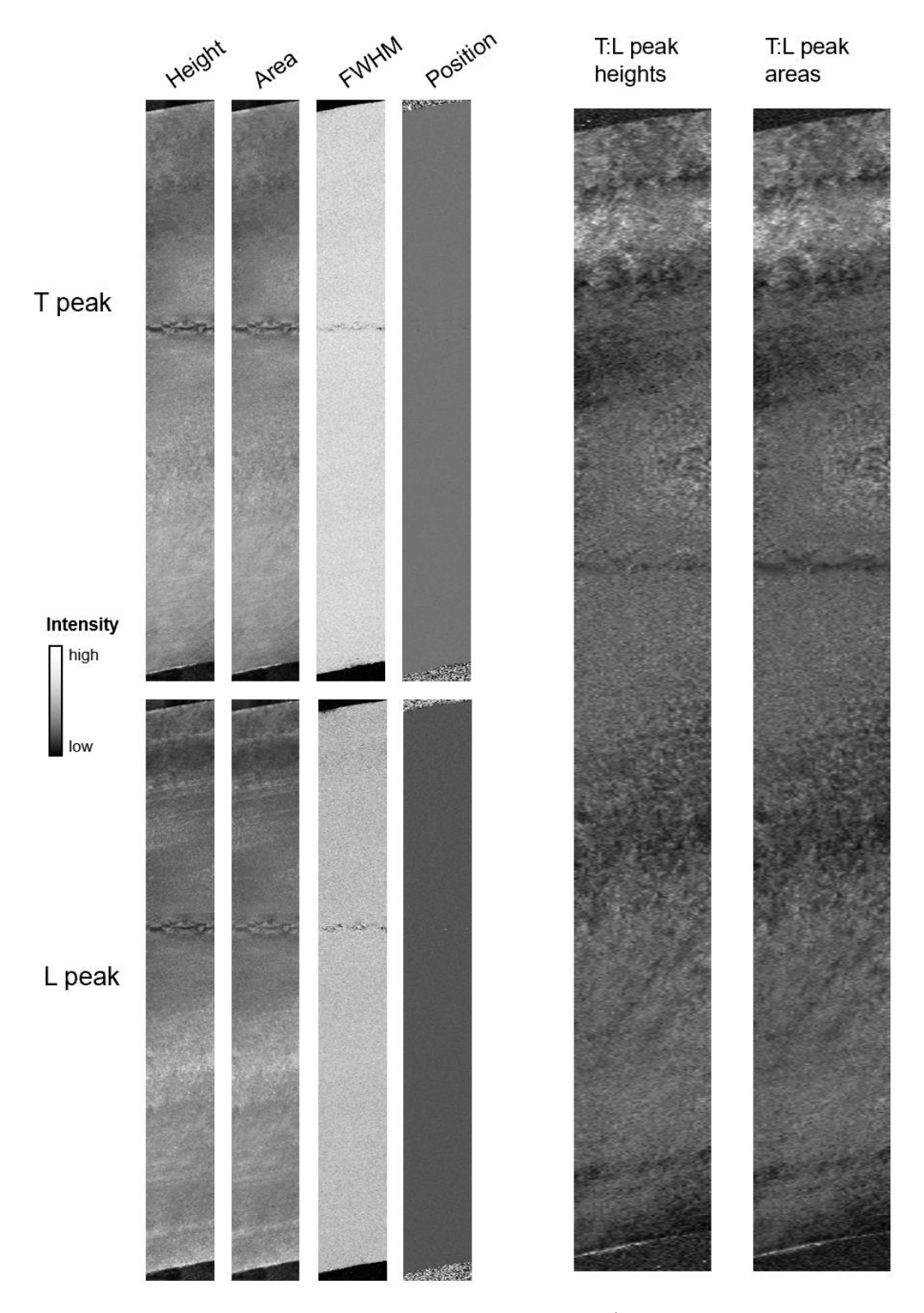


Figure S5. Raman maps of T (translation, 140–170 cm⁻¹) and L (libration, 200–220 cm⁻¹) mode peak parameters (height, area, FWHM, position) and the T:L peak height and area ratios of the freshwater pearl. Maps were collected at $3 \times 6 \mu m$ pixel step sizes with ~5 μm spot size resolution and the maps span $300 \times 2600 \mu m$.

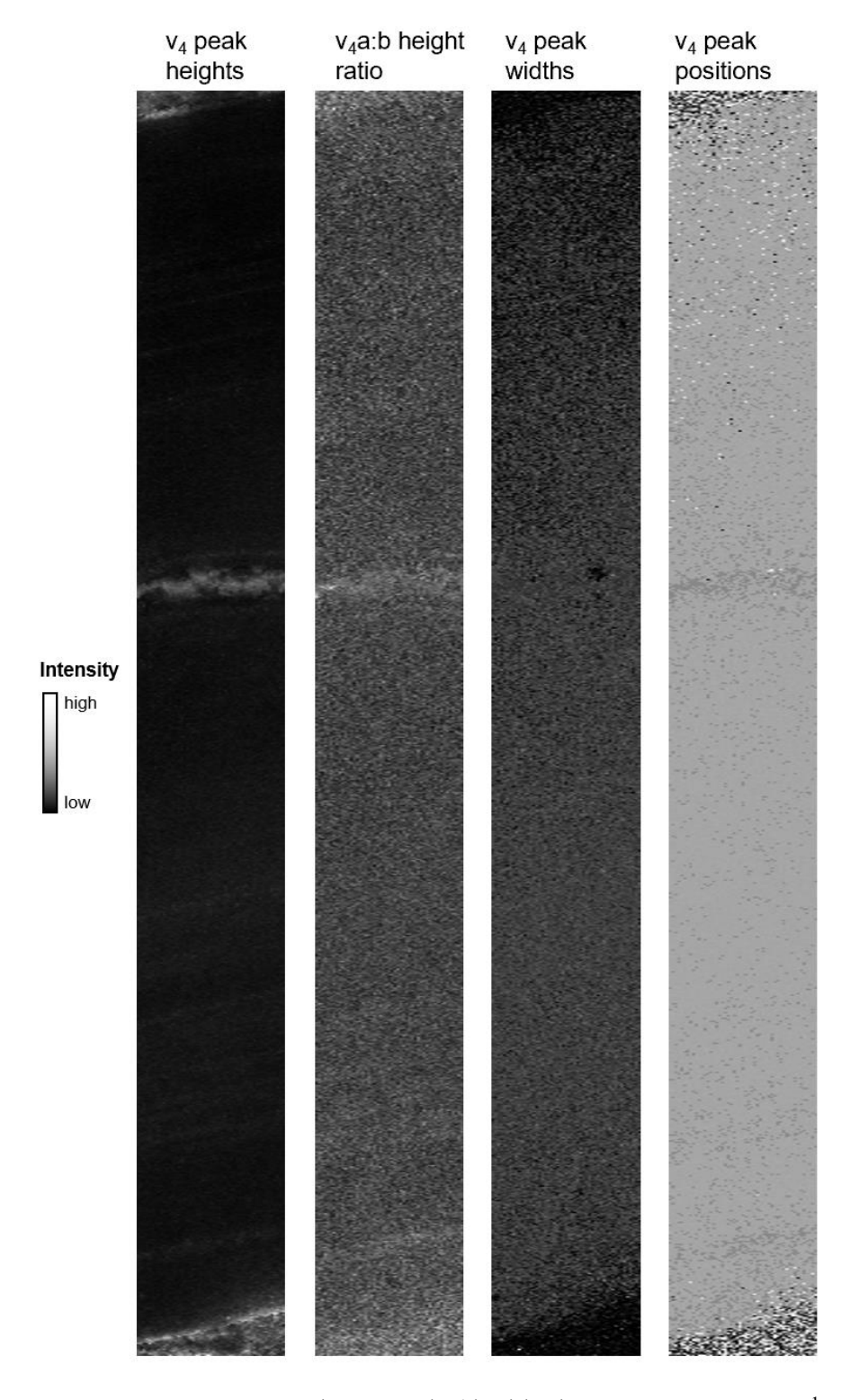


Figure S6. Raman maps the ν_4 mode (doublet between 698–710 cm⁻¹; ν_4 A= 698–704 cm⁻¹, ν_4 B= 704–710 cm⁻¹) peak parameters (height, area, FWHM, position) of the freshwater pearl. Maps were collected at 3 × 6 μ m pixel step sizes and the maps span 300 × 2600 μ m.

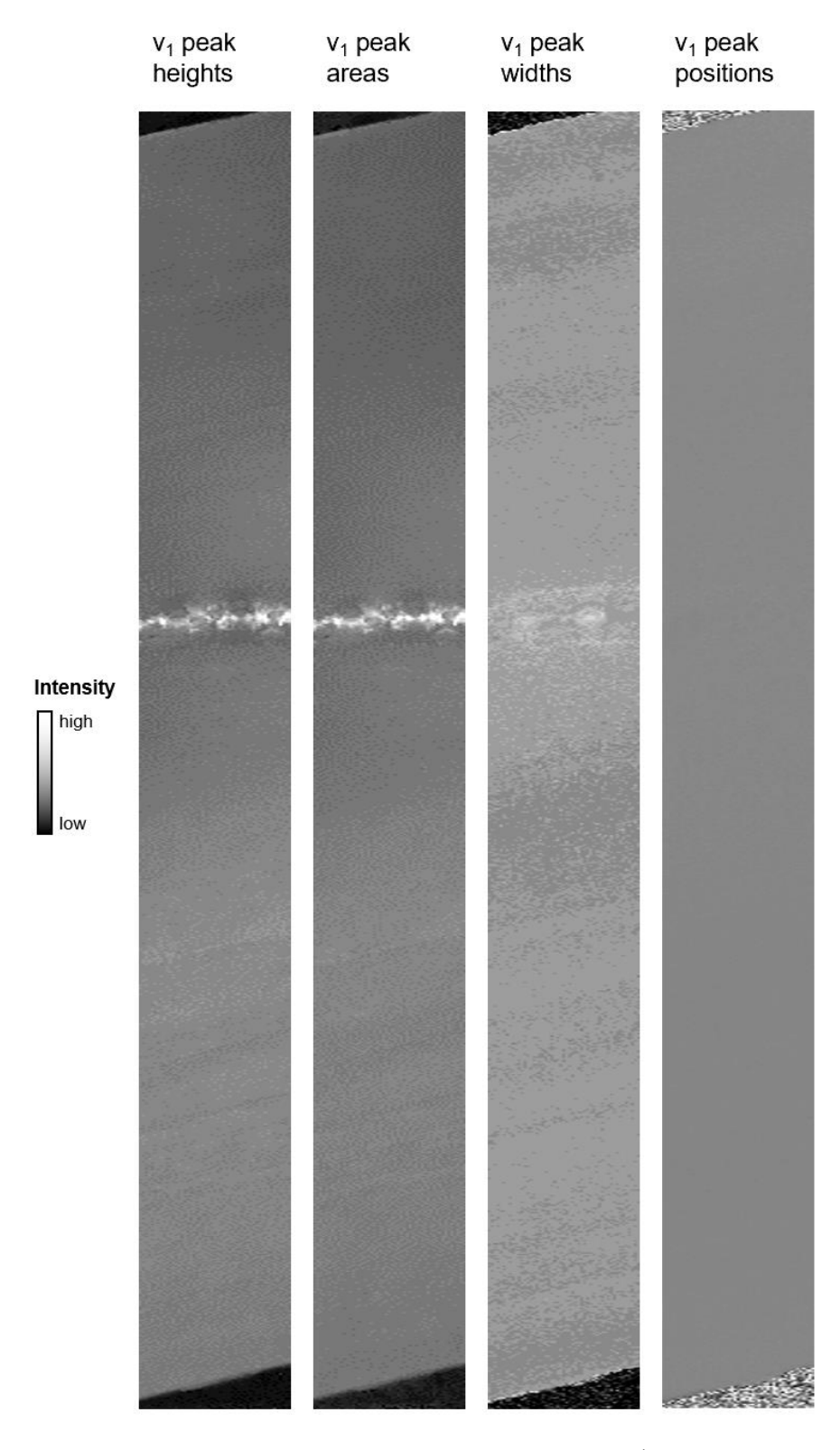


Figure S7. Raman maps the v_1 mode (1080–1090 cm⁻¹) peak parameters (height, area, FWHM, position) of the freshwater pearl. Maps were collected at 3×6 µm pixel step sizes and the maps span 300×2600 µm.

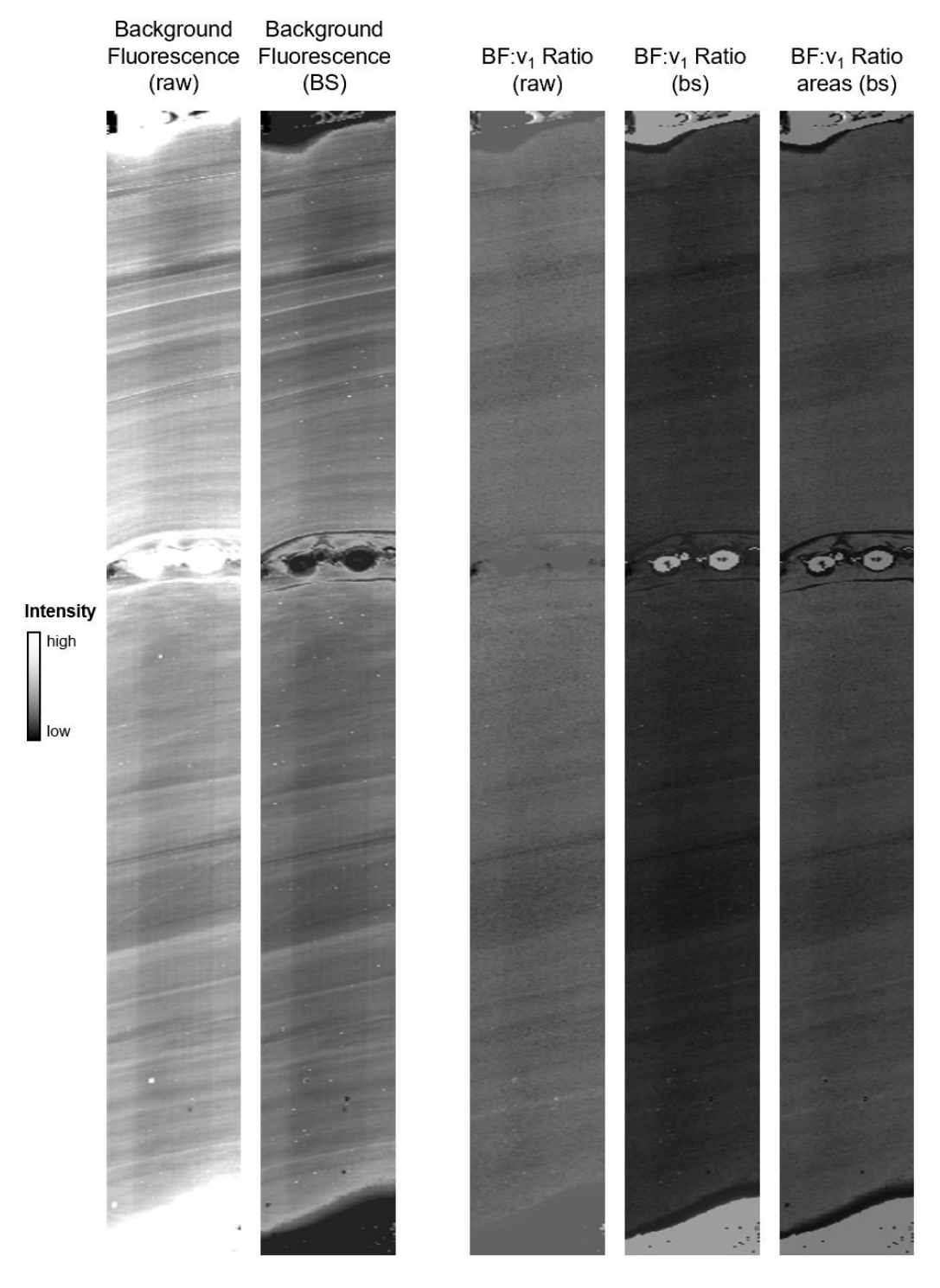


Figure S8. Raman maps of the background luminescence (fluorescence) presented in different ways (raw, background-subtracted with a linear background (BS), as a ratio with the v_1 mode height) of the freshwater pearl. Maps were collected at 3×6 µm pixel step sizes and the maps span 300×2600 µm.

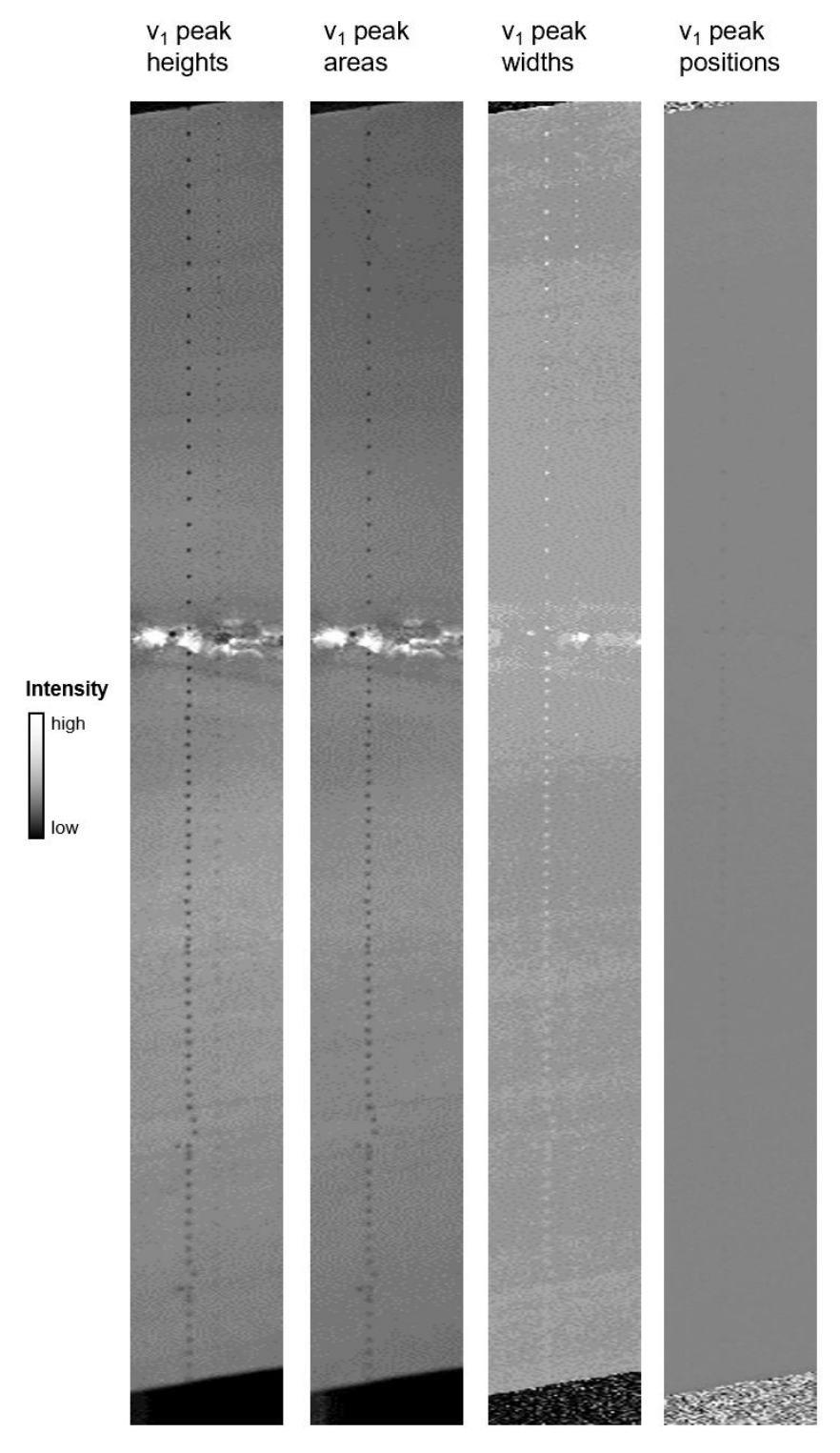


Figure S9. A duplicate Raman map of the v_1 mode peak parameters (height, area, FWHM, position) in an area adjacent to the area used for the other maps. This area is directly over the SIMS pits and EPMA spots of the freshwater pearl. Maps were collected at $3 \times 6 \mu m$ pixel step sizes and the maps span $300 \times 2600 \mu m$.

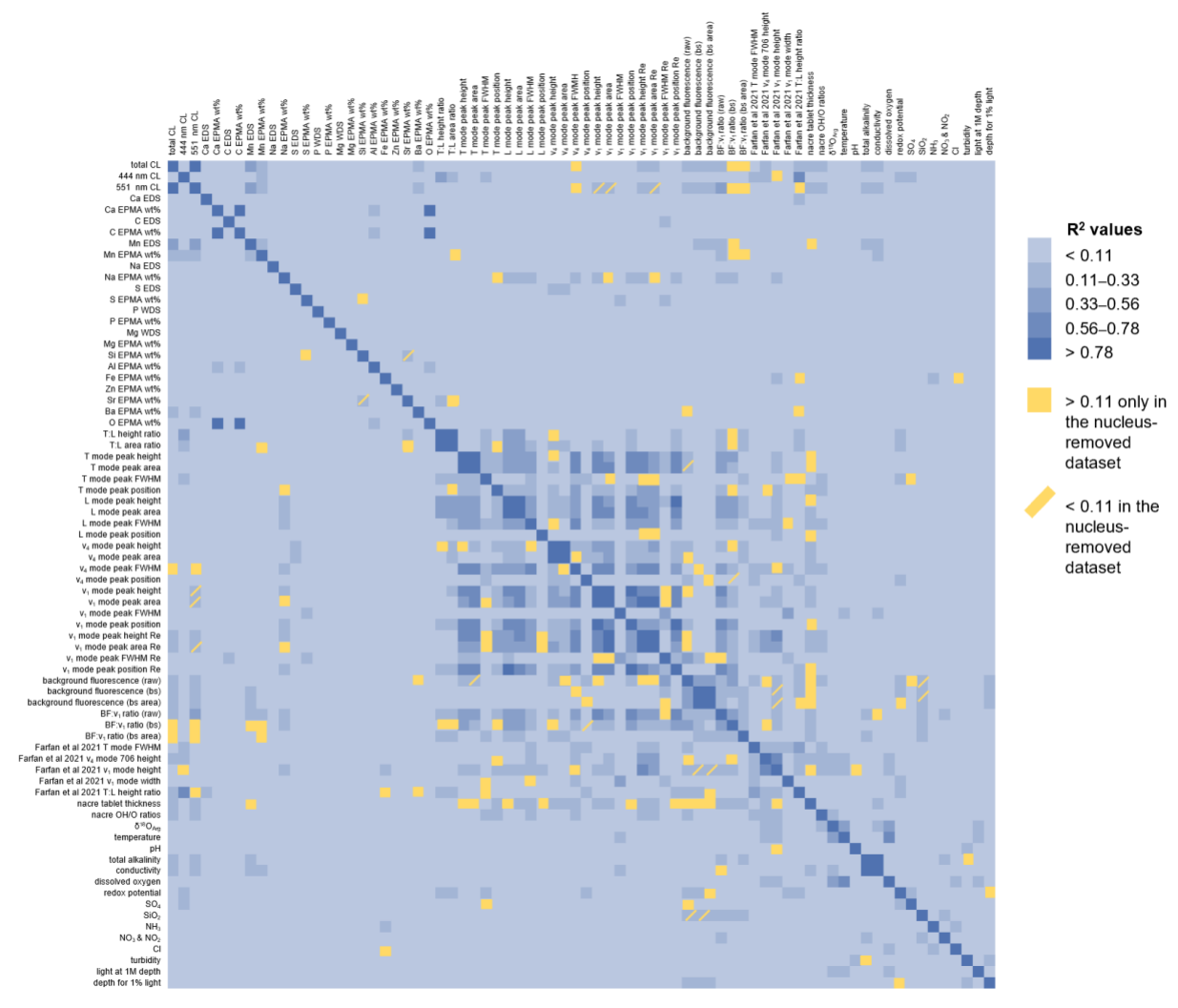


Figure S10. Coefficients of determination (R²) matrix of most variables in this study for the freshwater pearl sample, plus select mineralogical and environmental data from Farfan et al. 2021. Blue colors represent R² values for the full pearl transect and yellow colors represent differences between these trends and those seen in the pearl transect without the nucleus region (900-1100 cm⁻¹) included. For specific values, see Table S4.

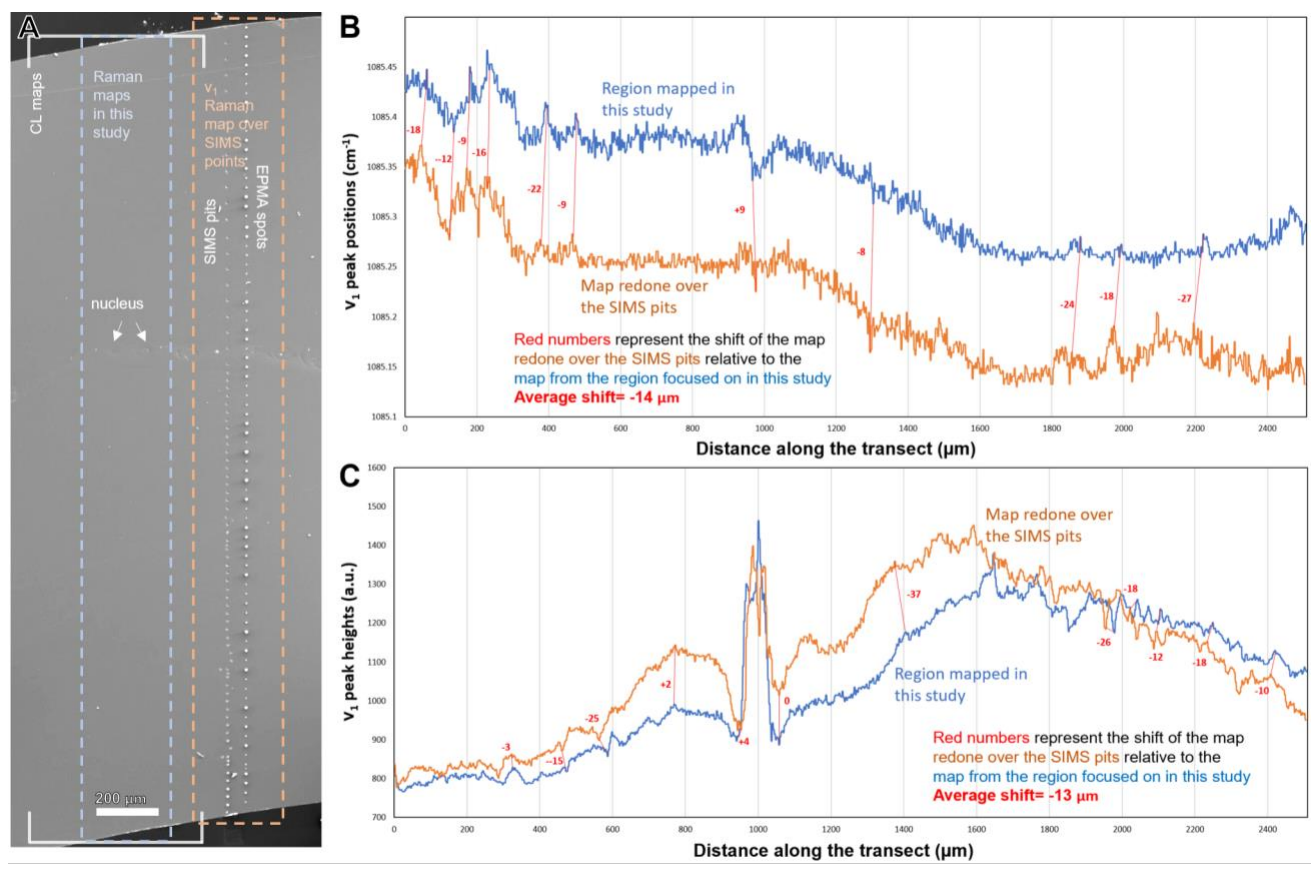


Figure S11. Comparing alignment offsets between Raman maps collected in the region of study (Fig. S7) versus in the adjacent region over the SIMS pits (Fig. S9). A) A secondary electron image of the freshwater pearl with the region of the Raman maps presented in the main text (Fig. S7) presented in blue dashed lines and the duplicate Raman map region collected over the SIMS pits (Fig. S9) outlined in orange dashed lines. B) Comparison of v_1 mode peak positions across the transect in the region presented in this study (blue) versus the duplicate map over the SIMS pits region. C) Comparison of v_1 mode peak heights across the transect in the region presented in this study (blue) versus the duplicate map over the SIMS pits region.

On average, the Raman map over the SIMS pits region (orange) is shifted down-transect by approximately 13 μm compared to the transect from the region presented in this study (blue). Across the transects, there are small shifts that occur randomly in both directions. Since there are no consistent shifts towards or away from the nucleus, this suggests that there is no substantial misalignment across the two regions. Considering that our results of the Mn and 551 CL peak maxima are offset 30–200 μm from the $\delta^{18}O_{Arg}$ maxima (compared to smaller offsets between these two Raman maps), and that those offsets are consistent on either side of the nucleus, suggests that the offsets between Mn and 551 CL peak maxima and $\delta^{18}O_{Arg}$ maxima are real and not artifacts due to misalignments.

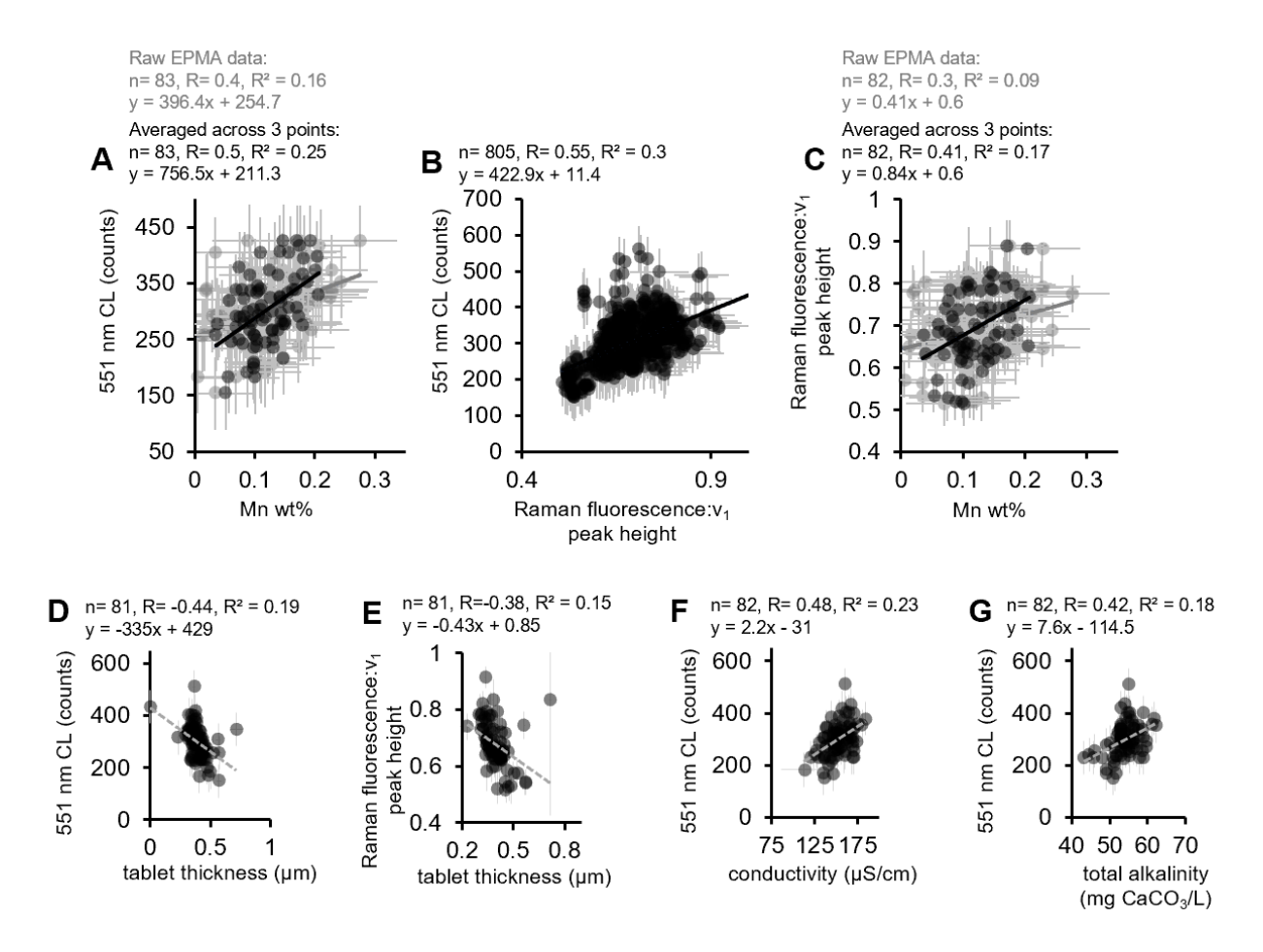


Figure S12. Pearson correlation plots between variables in this study and Farfan *et al.*, 2021 that are depicted as transects in Figure 5. Points are shown at 50% transparency.

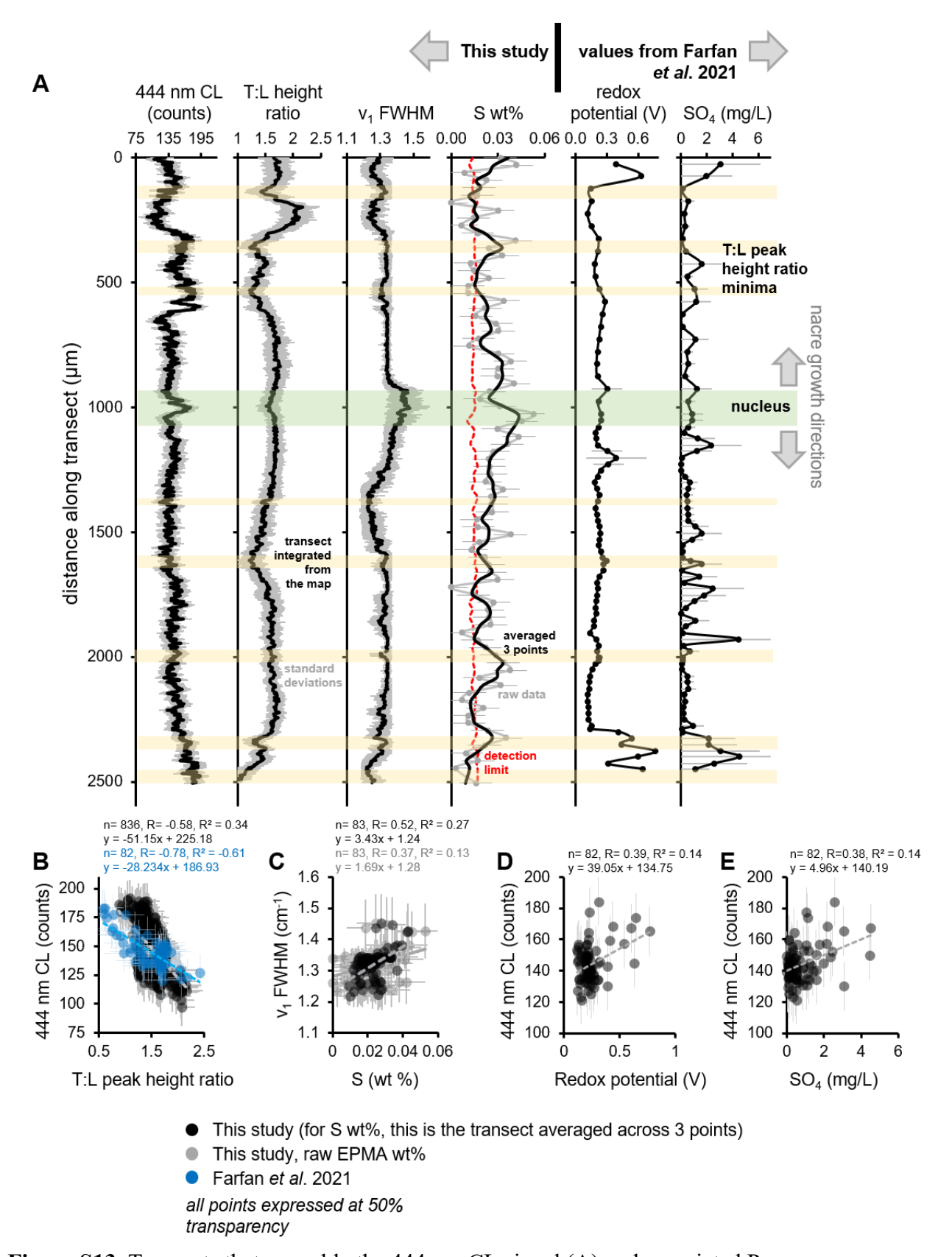


Figure S13. Transects that resemble the 444 nm CL signal (A) and associated Pearson

correlation plots (B-E) between variables in this study and Farfan *et al.*, 2021 of the freshwater pearl. In part A, yellow bars represent the T:L peak height ratio minima to show how the different variables align with each other.

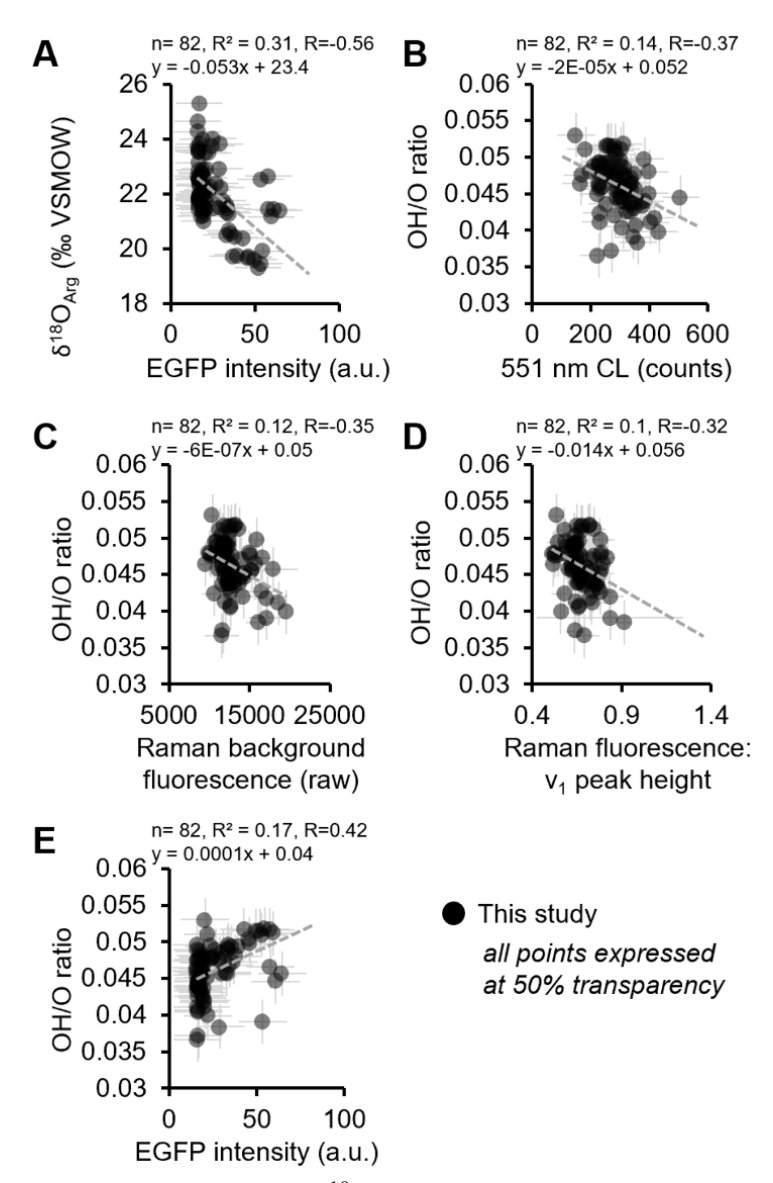


Figure S14. A) SIMS $\delta^{18}O_{Arg}$ measurements as a function of enhanced green fluorescent protein (EGFP) laser fluorescence intensity of the freshwater pearl. SIMS OH/O ratios correlated against B) 551 nm CL signals, C) raw Raman background fluorescence intensity, D) the ratio of Raman background fluorescence: peak heights (linear background-subtracted), and E) EGFP laser fluorescence intensity. Error bars represent measurement precision for SIMS data and standard deviations in measurements for the other variables.

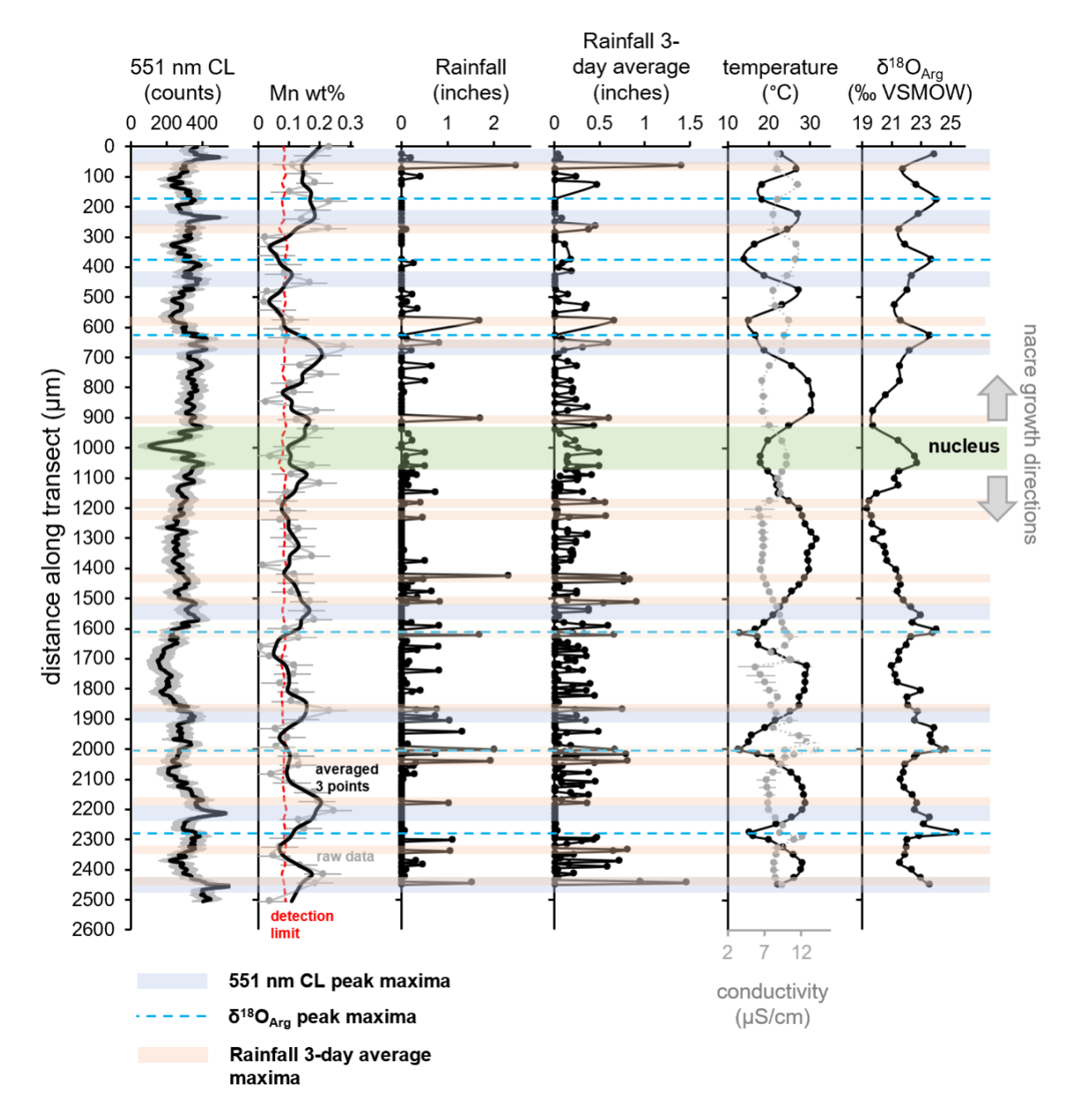


Figure S15. Rainfall records for nearby Paris, TN (NOAA Station USC00406977) compared to our 551 nm CL and Mn concentration data, as well as temperature and conductivity data for Kentucky Lake and nacre $\delta^{18}O_{Arg}$. Rainfall maxima (assumed to be rainstorms) are highlighted in orange bars and generally appear to precede Mn and CL peaks.

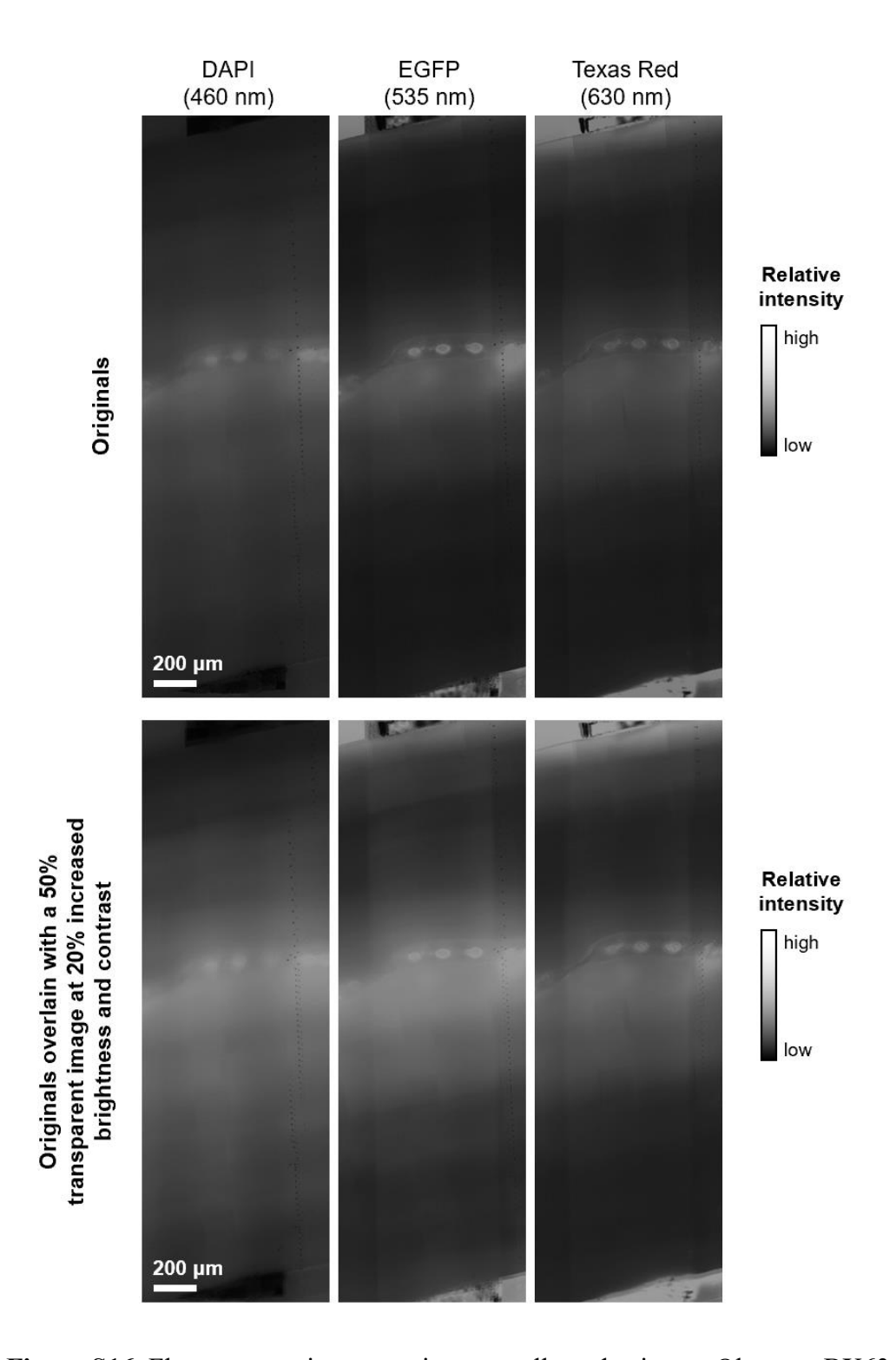


Figure S16. Fluorescent microscopy images collected using an Olympus BX63 microscope in mercury arc epi-illumination at 20× magnification and captured with an Olympus DP80 camera of the freshwater pearl. The auto fluorescent properties of the specimens were utilized to collect images using long bandpass filter cubes as follows: blue (DAPI) 325–375 nm excitation and 435–485 nm emission, green (EGFP–enhanced green fluorescent protein, FITC–fluorescein

isothiocyanate) 465–495 nm excitation and 515–555 nm emission, and red (Texas Red) 540–580 nm excitation and 600–660 nm emission. Images were stitched together using Olympus cellSens software. Original images are presented at the top and the bottom row represent the same images with altered brightness and contrast (created by superimposing a 50% transparent figure of the image at 20% increased brightness and contrast over the original figure, thus allowing for some of the details in the darker regions to show up more clearly). Transects of greyscale intensity of the images were calculated using ImageJ software (Schneider et al. 2012).

Reference: Schneider, C.A.; Rasband, W.S.; Eliceiri, K.W. 2012. NIH Image to ImageJ: 25 years of image analysis. Nat. Methods 9, 671–675.

A discussion of organics in freshwater pearl nacre—Raman background fluorescence, laser autofluorescence, and OH contents

SIMS-based nacre OH/O ratios have been proposed to represent relative amounts of organic or hydrous components in carbonates, yet it still unknown whether the OH in nacre represents organic molecules versus OH-groups or water trapped around the aragonite tablets (Orland et al., 2015; Linzmeier et al., 2016; Wycech et al., 2018). Here, we observe that OH/O ratios are negatively correlated with the 551 nm CL signal (Fig. S12B; R²=0.14, R= -0.37), Raman background fluorescence (raw) signals (Fig. S12C; R²=0.12, R= -0.35), and Raman background fluorescence:v₁ mode peak height ratios (Fig. S12D; R²=0.1, R= -0.32), and positively correlated with increasing tablet thickness (Farfan et al., 2021), suggesting that OH/O ratios are not associated with organics or emitters expressed by these types of measurements. To confirm that the fluorescent signals from Raman mostly represent organic contents, we also imaged the pearl using laser fluorescence with standard enhanced green fluorescent protein (EGFP), DAPI, and Texas Red filters and observed that the distribution of organics is most concentrated around the nucleus of the pearl but still broadly aligns with the Raman fluorescence signal (Fig. S12,S13; Orland et al., 2009; Wanamaker et al., 2009; Hoffman et al., 2016). OH/O values do positively correlate moderately with the EGFP laser fluorescence signals (Fig. S12E; $R^2=0.17$, R=0.42), indicating that EGFP and Raman fluorescence likely portray different emitters (such as different organic molecules), of which the $\delta^{18}O_{Arg}$ and OH/O ratios are most closely associated with the EGFP-associated components. Previous studies have suggested that the laser fluorescence-emitting macromolecules are associated with chitin polysaccharides and proteins in shells of bivalves and brachiopods, but more detailed descriptions of the specific compounds associated with these fluorescent signals remain unexplored (Pérez-Huerta et al., 2008; Wanamaker et al., 2009). Overall, correlations with EGFP fluorescence (Fig. S12A,E), the organics-correlated 551 nm CL signal (Fig. S12B), and Raman fluorescence (Fig. S12C,D) indicate that the possible influence of specific organic molecules (i.e., β-chitin, Asp-rich glycoproteins, and others described in Levi-Kalisman et al. (2001) on $\delta^{18}O_{Arg}$ and OH/O ratios warrants further investigation.

References:

Hoffmann, R., Richter, D. K., Neuser, R. D., Jöns, N., Linzmeier, B. J., Lemanis, R. E., Fusseis, F., Xiao, X, Immenhauser, A. 2016. Evidence for a composite organic—inorganic fabric of belemnite rostra: Implications for palaeoceanography and palaeoecology. Sedimen. Geol. 341, 203–215.

Linzmeier, B. J., Kozdon, R., Peters, S. E., Valley, J. W. 2016. Oxygen isotope variability within growth bands suggests daily depth migration behavior is recorded in Nautilus shell aragonite, PLoS One, 1–31

Orland, I. J., Bar-Matthews, M., Kita, N. T., Ayalon, A., Matthews, A., & Valley, J. W. 2009. Climate deterioration in the Eastern Mediterranean as revealed by ion microprobe analysis of a speleothem that grew from 2.2 to 0.9 ka in Soreq Cave, Israel. Quat. Res. 71(1), 27–35.

Orland, I. J., Kozdon, R., Linzmeier, B., Wycech, J., Sliwinski, M., Kitajima, K., Kita, N., Valley, J.W. *In* AGU Fall Meeting *Abstracts* 2015, Vol. *2015*, p. PP52B–03.

Pérez-Huerta, A., Cusack, M., Ball, A., Williams, C. T., Mackay, S. 2008. Deciphering the distribution of organic components in brachiopod shells by confocal laser scanning microscopy. J. Microsc. 230(1), 94–99.

Wycech, J., Kelly, D. C., Kozdon, R., Orland, I., Spero, H. J., Valley, J. W. 2018. Comparison of δ^{18} O analyses on individual planktic foraminifer (Orbulina universa) shells by SIMS and gassource mass spectrometry. Chem. Geol. 483, 119–130.

Wanamaker Jr, A. D., Baker, A., Butler, P. G., Richardson, C. A., Scourse, J. D., Ridgway, I., Reynolds, D. J. 2009. A novel method for imaging internal growth patterns in marine mollusks: A fluorescence case study on the aragonitic shell of the marine bivalve Arctica islandica (Linnaeus). Limnol. Oceanogr.: Methods 7(9), 673–681.

Table S1. Measurement details and standards for the wavelength-dispersive (WDS) analysis on the electron microprobe. O was calculated by stoichiometry, and CO₂ by difference from 100.

Element	WDS Crystal	Standard	Detection limit (ppmw)
Na	TAPL	Albite	60
Mg	TAPL	Dolomite	30
P	PETL	Fluor-apatite	130
S	PETL	BaSO ₄	130
Ca	PETL	Calcite	80
Si	TAPL	SiO ₂	60
Al	TAPL	Al ₂ O ₃	35
Fe	LIFL	Siderite	160
Mn	LIFL	MnO_2	140
Zn	LIFL	K253 (NIST glass)	280
Sr	PETH	Strontianite	210
Ba	PETH	BaSO ₄	170